Published in final edited form as:
J Adv Model Earth Syst. 2017 June ; 9(2): 790–809. doi:10.1002/2016MS000836.

The impact of simulated mesoscale convective systems on global precipitation: A multiscale modeling study

Wei-Kuo Tao[1], **Jiun-Dar Chern**[2]

[1]Mesoscale Atmospheric Processes Laboratory, NASA Goddard Space Flight Center, Greenbelt, Maryland, USA,

[2]Earth System Science Interdisciplinary Center, University of Maryland, College Park, Maryland, USA

Abstract

The importance of precipitating mesoscale convective systems (MCSs) has been quantified from TRMM precipitation radar and microwave imager retrievals. MCSs generate more than 50% of the rainfall in most tropical regions. MCSs usually have horizontal scales of a few hundred kilometers (km); therefore, a large domain with several hundred km is required for realistic simulations of MCSs in cloud-resolving models (CRMs). Almost all traditional global and climate models do not have adequate parameterizations to represent MCSs. Typical multiscale modeling frameworks (MMFs) may also lack the resolution (4 km grid spacing) and domain size (128 km) to realistically simulate MCSs. The impact of MCSs on precipitation is examined by conducting model simulations using the Goddard Cumulus Ensemble (GCE, a CRM) model and Goddard MMF that uses the GCEs as its embedded CRMs. Both models can realistically simulate MCSs with more grid points (i.e., 128 and 256) and higher resolutions (1 or 2 km) compared to those simulations with fewer grid points (i.e., 32 and 64) and low resolution (4 km). The modeling results also show the strengths of the Hadley circulations, mean zonal and regional vertical velocities, surface evaporation, and amount of surface rainfall are weaker or reduced in the Goddard MMF when using more CRM grid points and higher CRM resolution. In addition, the results indicate that large-scale surface evaporation and wind feedback are key processes for determining the surface rainfall amount in the GMMF. A sensitivity test with reduced sea surface temperatures shows both reduced surface rainfall and evaporation.

1. Introduction

Continued advancements in computational technology now allow general circulation models (GCMs) to begin to resolve individual convective clouds and convective systems. Though still computationally very demanding (~ a million times more than a traditional GCM), global cloud-resolving (or cloud-permitting) models (GCRMs) with horizontal grid spacing from 870 m to 14 km have been successfully used in many short-term atmospheric studies

Correspondence to: W.-K. Tao, Wei-Kuo.Tao-1@nasa.gov.

[e.g., *Tomita et al.*, 2005; *Satoh et al.*, 2005, 2008, 2014; *Putman and Suarez*, 2011; *Miyamoto et al.*, 2013; *Skamarock et al.*, 2014; *Yashiro et al.*, 2016] as well as a long-term (20 years with 14 km resolution) climate simulation [*Kodama et al.*, 2015]. Another more economical approach to global cloud-resolving (or cloud-permitting) modeling is the multiscale modeling framework (MMF) wherein conventional cloud parameterizations are replaced with a cloud-resolving model (CRM) in each grid column of a GCM [*Grabowski and Smolarkiewicz*, 1999; *Khairoutdinov and Randall*, 2001; *Khairoutdinov et al.*, 2005; *Randall et al.*, 2003; *Tao et al.*, 2009, and papers listed in Table 1]. An MMF can explicitly simulate deep convection, cloudiness and cloud overlap, and cloud-radiation interactions at the resolution of a CRM. It expands traditional CRM modeling to a global coverage and enables two-way interactions between the cloud and large scales.

The first MMF [called the Superparameterized Community Atmosphere Model (SPCAM)] was developed at Colorado State University (CSU) [*Khairoutdinov and Randall* 2001; *Randall et al.*, 2003], using the System for Atmospheric Modeling (SAM, a CRM) to replace the convection parameterizations in the National Center for Atmospheric Research (NCAR) Community Atmosphere Model (CAM). It has been used to study a wide variety of atmospheric phenomena and a review of the major applications can be found in *Randall et al.* [2016]. A second MMF [*Tao et al.*, 2009] has been developed at Goddard with a different GCM [the Goddard Earth Observing System (GEOS) model] and a different CRM [the Goddard Cumulus Ensemble model (GCE)]. Recently, a new Goddard 4ICE (cloud ice, snow, graupel, and hail) scheme was implemented into the Goddard MMF (GMMF) [*Chern et al.*, 2016]. The 4ICE scheme improves the GMMF-simulated cloud ice spatial patterns and amount as compared to CloudSat estimates. It also shows improved performance with respect to the land-ocean contrast in precipitating cloud frequencies and microphysics in relations to the TRMM products and results from a GCRM [*Matsui et al.*, 2016]. GMMF simulations with the improved 4ICE scheme were incorporated into a satellite-retrieval database for the cross-track scanning sensors of the Global Precipitation Measurement (GPM) constellation satellites [*Kidd et al.*, 2016].

Khairoutdinov and Randall [2003] tested the sensitivity of their CRM (SAM) to domain size (from 512 to 9192 km) and horizontal resolution (from 250 m to 32 km). Their 20 member ensemble runs were forced by large-scale advective tendencies in temperature and water vapor from an intensive observation period conducted over Oklahoma in 1997 at the ARM/SGP (DOE Atmospheric Radiation Measurement Program/Southern Great Plains) site. They found that the mean simulation statistics had very little sensitivity to the model domain size. They also found that the simulated hydrometeor mixing ratios and cloud fraction profiles had virtually no sensitivity to grid resolution as long as it was finer than 4 km. Their conclusions are one of the main reasons why nearly all MMFs applied a 4 km grid in their embedded CRMs (see Table 1).

The importance of mesoscale convective systems (MCSs) on tropical precipitation was identified [*Houze*, 1982, 1989] and quantified from TRMM precipitation radar and microwave imager retrievals [*Nesbitt et al.*, 2006] and CRMs [see Table 1 in *Cotton et al.*, 1995]. MCSs generate more than 50% of the rainfall in most tropical regions. Typical MCSs have a horizontal scale of a few hundred kilometers. *Johnson et al.* [2002] used large-scale

advective tendencies for temperature and water vapor obtained from TOGA COARE (the Tropical Ocean Global Atmosphere-Coupled Ocean Atmosphere Response Experiment) to force the GCE. Their results indicated that a domain size of at least 512 km is needed to adequately contain "mesoscale convective features" and to replicate both the eastward and westward movements of the observed precipitating systems. *Tompkins* [2000] and *Petch and Gray* [2001] also indicated the importance of mesoscale organization in their TOGA COARE CRM simulations. Computationally, it is still quite expensive to use a 512 km domain size with 1 or 2 km grid spacing in the embedded CRMs of an MMF. In addition, *Ooyama* [2001] used a two-dimensional nonhydrostatic model to test the sensitivity of an isolated convective cloud and a squall line to resolution (1, 2, and 4 km). His results suggested that a resolution of 1 km or less, or marginally 2 km, is needed to realistically simulate precipitating clouds and squall lines.

Table 1 shows a list of MMF papers and their model configurations, such as their GCM resolution, the resolution and number of grid points in their CRMs, and length of model integration. Most MMFs used 32 or 64 grid points with 4 km grid spacing in their embedded CRMs. Only a few MMF studies [e.g., *Marchand and Ackerman*, 2010; *Pritchard et al.*, 2011] used 1 km grid spacing. See *Chern et al.* [2016] and *Randall et al.* [2016] for a review of these MMF papers in terms of their development, improvements and applications.

In this study, GMMF sensitivity tests were conducted to examine the impact of number of CRM grids and their resolution on model simulations. Specifically, the physical processes that can cause excessive rainfall over the West Pacific and other tropical oceans are the focus of the study. The paper has the following organization. Section 2 describes the GMMF, the Goddard microphysical schemes, and sensitivity tests. Section 3 shows the results of the numerical experiments assessing the impact of model configuration on surface rainfall. Section 4 offers a summary and conclusions.

2. Model Descriptions and Numerical Experiments

2.1. The Goddard MMF (GMMF)

The GMMF used in this study is the same as in *Chern et al.* [2016]. Briefly, the moist processes, radiation, and turbulence schemes in the GEOS global atmospheric model have been replaced with a two-dimensional (*x-z*) GCE [*Tao et al.*, 2014]. The GEOS model was configured to run with 2° × 2.5° (latitude × longitude) horizontal grid spacing with 48 vertical layers stretching from the surface to 0.4 hPa. In this study, a series of simulations were carried out with differing numbers of GCE grid columns (i.e., 32, 128, 64, and 256) and grid spacing (i.e., 1, 2, and 4 km). All embedded GCEs have 44 vertical layers and time steps of 3, 6, and 12 s for model resolutions of 1, 2, and 4 km, respectively. In the GMMF, the GCE is in a height coordinate, and the model height does not change with time (different from SPCAM's approach). Therefore, the vertical levels are slightly different between GEOS and GCE to ensure the model top height in the GCE is lower than that of GEOS. Prescribed sea surface temperatures (SSTs) from NOAA OI weekly SSTs [*Reynolds et al.*, 2007] were used, while the initial atmospheric conditions were taken from the ECMWF ERA-Interim reanalysis [*Dee et al.*, 2011] at 0000 UTC 1 December 2006. The first month was considered as spin-up, and only results from 2007 and 2008 were depicted in this paper.

In this study, the surface fluxes are computed from the GCM grids based on the GCM's lowest-level fields and are used as constant fluxes (horizontally uniform) in the embedded CRM. The representation of convective momentum transport (CMT) in an MMF has been a long-standing challenge due to the 2-D nature of the embedded CRMs. The GMMF is like other traditional MMFs in only considering the thermodynamic feedback.

Most CRM microphysical schemes include two liquid (cloud water and rain) and three classes of ice particles (cloud ice, snow, and graupel or hail) [see Table 1 in *Tao et al.*, 2016]. However, graupel and hail can co-exist in real clouds. Therefore, the Goddard 3ICE scheme was improved by including both graupel and hail (called the Goddard 4ICE scheme, see *Lang et al.* [2014]). The Goddard 4ICE scheme was also implemented into the NASA Unified Weather Research and Forecasting model (NU-WRF), which significantly improved the simulation of heavy rainfall associated with a midlatitude squall line [*Tao et al.*, 2016]. The 4ICE scheme improves the GCE and NU-WRF radar signatures in two ways: (1) it eliminates the occurrence of elevated reflectivity maxima (most likely via higher hail fall speeds) and still works well for less intense cases, and (2) with its ability to produce high reflectivity values, it eliminates the need for graupel and snow to produce those values, allowing for more "stable" snow/graupel size mappings and mappings better suited to produce reflectivity values with the highest occurrence.

2.2. Model Configuration and Sensitivity Tests

Table 2 lists four GMMF sensitivity tests. The first two sensitivity tests (M32 and M64) used 32 and 64 CRM grid columns with 4 km grid spacing, respectively. These model configurations are frequently used in MMF simulations (see Table 1). The next two sensitivity tests (M128 and M256) used 128 and 256 CRM grid columns with 2 and 1 km grid spacing, respectively. The embedded CRMs have an east-west orientation. Note that the M64, M128, and M256 configurations have the same domain size (256 km), which is similar to the GEOS longitudinal grid spacing (2.5°). Most previous MMF studies (Table 1) used embedded CRMs with a domain size of 128 and 4 km grid spacing, which matches and is the justification for the M32 simulation. It is worth noting that the majority of organized tropical convective systems are over 100 km in size [*Nesbitt et al.*, 2006]. These two tests are designed to examine whether simulated convection is more or less organized than the two tests with less grid columns.

In addition to the GMMF simulations, four CRM (GCE) simulations (i.e., C32, C64, C128, and C256 in Table 2) are conducted. The same CRM configurations used in the GMMF runs are used in these CRM simulations. Large-scale advective forcing in temperature and water vapor is used to derive these CRM simulations. These off-line (noninteractive with GEOS) simulations are used to examine the sensitivity of CRM configurations on surface precipitation and the degree of convective organization. The 4ICE scheme is used in both GCE and GMMF for all experiments in this study.

3. Results

3.1. CRM Simulations

The GCE is used to examine the sensitivity of stand-alone 2-D CRM simulations without cloud-large-scale interaction to horizontal resolution and domain size. The observed large-scale forcing in temperature and water vapor from 20 to 30 November 2011 during the Dynamics of the Madden-Julian Oscillation (MJO) (DYNAMO) [*Yoneyama et al.*, 2013] field campaign is used to drive the simulations (i.e., C32, C64, C128, and C256). Surface rainfall retrieved by the ground-based S-band dual-polarized (S-POL) radar located at Gan Island was used to constrain the forcing. Since there was only a single sounding site at Gan Island, ECMWF global analyses were used to provide temperature, water vapor, and wind profiles near the Gan site. Table 3 shows the convective, stratiform, and total rainfall, its stratiform percentage, temporal correlation as well as the domain-mean rainfall bias for these four simulations. The convective and stratiform separation method considers the surface rainfall intensity, middle-level vertical velocity, and low-level cloud water (100% saturated with presence of cloud water). See *Tao et al.* [1993] and *Lang et al.* [2003] for more details on the separation method. All of the runs produced similar rainfall totals (from 12.86 to 13.37 mm d^{-1}) in good agreement with the observed (13.03 mm d^{-1}). This is because the runs were all constrained by the prescribed large-scale advective forcing in temperature and water vapor.

The C32 and C64 runs both used the same 4 km grid spacing, but the C64 simulation had slightly more convective and stratiform rainfall (Table 3). The results also showed that both the C32 and C64 runs simulated the same 57% stratiform rainfall amount. The C128 and C256 cases both produced more convective but less stratiform rainfall and hence a slightly lower stratiform percentage (53%) than the C32 and C64 cases. The C256 experiment had the highest correlation (0.90) of all and a lower bias (0.23) than the C64 and C128 runs. The C32 simulation had the lowest correlation (0.73) and a negative bias compared to the others.

Figure 1 shows time series of the domain-mean rainfall for the C32, C64, C128, and C256 simulations. All four runs capture the observed temporal variation in rainfall, especially the heavy rainfall events (i.e., on November 23, 24, 25, 26, 27, and 28). However, the C32 run generally overestimates the peak intensity of these heavy rainfall events while underestimating their life span compared to the observations and other simulations. The C64 and C128 runs are both better than the C32 case in this regard with C128 being slightly better than the C64 during the first 4 days of model integration. The C256 simulation, however, clearly shows the best agreement with the observed temporal variation in domain-mean surface rainfall in agreement with the high correlation and low bias shown in Table 3.

Hovmoller diagrams of model-simulated hourly rainfall for the C32, C64, C128, and C256 simulations are shown in Figure 2. The C32 run produces short-lived, isolated convection with large rainfall intensities (especially between 20–21 November and 25–28 November) compared to the other runs. Its simulated domain-mean rainfall period is also shorter than the other cases as shown in the Figure 1a. The C256 simulation has more long-lived organized convection, and its simulated domain-mean rainfall is in very good agreement with the observed as shown in Figure 1d. In addition, the C256 run produces finer, more-

detailed structures than the C32. The C128 run has slightly more long-lived, organized convection than does C64 between 25 November and 27 November (see Figures 1 and 2c) and slightly better correlation overall (Table 3).

Figure 3 shows vertical cross sections of simulated radar reflectivity from the four CRM simulations. In general, more complex cloud structures are seen in the C256 (1 km resolution) and C128 (2 km resolution) simulation. Convective cell structures appear broader for the C32 and C64 simulations (see Figures 3a and 3b). These results are in good agreement with *Ooyama* [2001]. The time series of maximum vertical velocity and maximum radar reflectivity are also examined (not shown). The peak intensity of radar reflectivity is about 45–50 dBZ in all GCE experiments (see Figure 3). These values are located beneath the melting layer. The maximum updraft (grid point value) is stronger (weaker) in the high (low)-resolution case as expected. For example, the maximum updraft is about 8 m s^{-1} in the C32 configuration but reaches over 12 m s^{-1} in the C256 case. Another difference is that stronger updrafts last longer (shorter) in the C256 (C32) case as multiconvective cores are simulated in C256 (see Figure 3). This result is consistent with the rainfall (Figure 1).

3.2. GMMF Simulations

GMMF simulations were conducted for 2 years, 1 January 2007 to 31 December 2008. These same 2 years were used to compare the GMMF M32 simulation with CloudSat products in *Chern et al.* [2016]. In this paper, GMMF-simulated rainfall characteristics will be compared for different model configurations. The Global Precipitation Climatology Project (GPCP) [*Adler et al.*, 2003] and two Tropical Rainfall Measuring Mission (TRMM) [*Simpson et al.*, 1996] products [*Huffman et al.*, 2007, 2010] are used to evaluate model performance. The GPCP data have global coverage at 2.5° resolution, the TRMM 3B43 merged product covers from 50°S to 50°N at 0.25° resolution, and the TRMM 3A25 Precipitation Radar (PR) gridded product covers from 38°S to 38°N at 0.5° resolution. All data sets are averaged to the model grids at 2.0° × 2.5° resolution for comparison.

The GCE model configurations used in the M32, M64, M128, and M256 experiments are the same as those in the C32, C64, C128, and C256 simulations, respectively, except now the GCE models can interact with the global circulation model (GEOS). Therefore, they do not have the same large-scale advective forcing (or vertical shear of horizontal wind) as their counterparts. Figure 4 shows the 2 year mean surface rainfall simulated in the M32, M64, M128, and M256 runs. The satellite surface rainfall estimates from the TRMM 3B43 and GPCP version 2.2 products are also shown in Figure 4 for comparison. All of the MMF-simulated rainfall patterns are quite similar to each other and to the satellite retrievals. For example, the minimum rainfall regions off the west coasts of North and South America and over subtropical Africa and the Atlantic are captured by all four simulations. In addition, four major rainfall features/regions, such as the Intertropical Convergence Zone (ITCZ), South Pacific Convergence Zone (SPCZ), Indian Ocean, and West Atlantic are also well captured by the GMMF runs. However, all four runs still simulate more rainfall than is estimated by satellite in these major rainfall regions. However, the results clearly indicate that the M128 and M256 runs produce less total rainfall over these regions than do the M32

and M64 runs, making them in better agreement with the satellite observations. Figure 5 shows the zonal mean rainfall differences between the four GMMF simulations and GPCP and TRMM 3B43. The biggest differences between the simulations and satellites observations are over the Tropics. The maximum zonal mean bias for the M256 simulation is noticeably less than for the M32 (1.4 mm d^{-1} versus 2.2 mm d^{-1} compared to GPCP and 1.9 mm d^{-1} versus 2.8 mm d^{-1} compared to TRMM in the Tropics). Overall, the M256 run has the least difference in (zonal-mean) rainfall compared to both TRMM and GPCP. The M64 and M128 runs also have smaller differences than does the M32.

The total rainfall amount, its bias, root-mean-square error (RMSE) and correlation for the four GMMF experiments are shown in Table 4. The convective and stratiform rainfall amount and stratiform percentage from each run are also shown. The M256 run has the lowest total rainfall amount, 2.83 (3.12) mm d^{-1}, the smallest bias 0.17 (0.22) and RMSE 1.37 (1.42), and the highest spatial correlation 0.842 (0.857) compared to GPCP (TRMM 3A25) among all runs. In contrast, the M32 simulation has the largest total rainfall amount, 2.93 (3.27) mm d^{-1}, the largest bias 0.27 (0.36) and RMSE 1.74 (1.85) as well as the smallest correlation 0.817 (0.825) of the runs relative to GPCP (TRMM 3A25). The M64 simulation has a better bias, RMSE and correlation than the M32. The M128 run produces the second best results and implies that CRMs with 128 grid points could be embedded into the GMMF and still achieve better agreement (reduced bias/RMSE and increased correlation) with observed rainfall than the current default setup.

The domain size of the CRM is typically chosen to be equal to or smaller than the parent GCM's grid spacing (~2°) in an MMF setup such as with the M32, M64, M128, and M256 experiments. However, a CRM domain size of 256 km (~2°) may be smaller than that necessary (i.e., 512 km) to adequately simulate tropical MCSs as suggested from previous stand-alone CRM simulations [*Tompkins*, 2000; *Johnson et al.*, 2002; *Petch and Gray*, 2001]. Therefore, an additional M128 configuration with 4 km grid spacing (i.e., a domain size of 512 km) was carried out; its global mean precipitation (not shown) has a bias/RMSE/correlation of 0.21/1.47/0.82, which are better than the GMMF runs (i.e., M32 and M64) with the same CRM grid spacing but smaller domains (i.e., 128 and 256 km). This result indicates that expanding the CRM domain to 2 times that of a typical parent GCM grid box (2.5° × 2°) can allow for more realistic MCS circulations and thereby reduce the artificial impacts of cyclic boundary conditions. However, the precipitation statistics for this additional test (i.e., 512 km domain size) are slightly worse than the M128 run with a higher resolution but smaller domain.

The M32 and M64 simulations typically produce one isolated cloud or cloud system as compared to the M128 and M256, which tend to produce more organized multicellar convective systems (see Figure 6). For example, Figure 6d shows an organized MCS with strong updrafts at the leading edge of the system and weaker updraft trailing behind (associated with a decaying convective cell). The updrafts are also stronger and penetrate to higher altitudes than those in the M32 and M64 runs (Figures 6a and 6b). Note that propagating convective cell(s)/system(s) exit from one lateral boundary and reenter on the other side due to the cyclic lateral boundary conditions.

The GMMF results are quite consistent with those from the uncoupled GCE runs. For example, the runs with 256 grid points (M256 and C256) have a low total rainfall bias and high spatial correlation compared to those with fewer grid points. In addition, the M256 and C256 runs simulate more organized MCSs compared to the M32 and C32. Both the M128 and C128 runs also have better bias results and correlations compared to their M64 and C64 counterparts. Overall, for both the GMMF and GCE model, simulations with the least number of model grid points have the worst performance in terms of simulated rainfall (Figures 1, 4, and 5).

All of the GCE and GMMF simulations produce a large stratiform rain percentage (from 51% to 63%, see Tables 3 and 4). The M32 and M64 runs simulated lower stratiform rain fractions, 55% and 51%, respectively, than the M128 and M256. These results are consistent with the more organized clouds/cloud systems in the M128 and M256 simulations. On the other hand, the C128 and C256 runs produced 4% lower stratiform fractions than the C32 and C64 (Table 3) even though there are more organized convective systems in the C128 and C256 simulations (Figure 3). This result is one of the differences between the GMMF and GCE simulations. Note that identical large-scale advective forcing with nudged horizontal winds was used to drive the uncoupled GCE experiments. Also, *Lang et al*. [2003] compared different convective-stratiform separation methods in the GCE model. Their results showed that the GCE-based (used in this paper) separation method could produce a higher stratiform (or less convective) fraction compared to the radar reflectivity-based method [*Steiner et al*., 1995].

Only one MMF study [*Cheng and Xu*, 2011] showed that simulated surface rainfall (SPCAM3.5) was under-predicted compared to observations [*Legates and Willmott*, 1990; see Figure 11 in *Cheng and Xu*, 2011]. However, in that study, the results were not compared with TRMM and/or GPCP as in other MMF studies (shown in Table 1). *Marchand and Ackerman* [2010] conducted three SPCAM simulations with different horizontal resolutions/vertical levels (i.e., 4 km/L26, 1km/L26, and 1km/L52, respectively). The 1 km simulations were only integrated for 1 month (November 2006). Their analysis only focused on cloud amount (not surface rainfall); they found the 1 km/L52 setup modestly improved the MMF-simulated low-cloud cover. *Pritchard et al*. [2014] also examined the impact of grid spacing on MJO dynamics in the SPCAM. Three CRM configurations (128 km long with 32 columns, 64 km long with 16 columns, and 32 km long with 8 columns) were integrated in SPCAM for a 10 year period (1980–1990). Their three simulations produced less rainfall on the equator and too much off of it (i.e., North Indian Ocean, Bay of Bengal, and northwestern tropical Pacific). The two configurations with reduced CRM domain sizes produced more rainfall on the Equator and slightly less rainfall in the Indian Ocean and SPCZ (see Figure 7 in their paper). *Pritchard et al*.'s results differ from this study as all of the GMMF runs produce too much rainfall along the Equatorial ITCZ and over the SPCZ and Indian Ocean. The differences could be caused by differences in the physics as well as the configuration tests between their study and this one.

3.3. Process Diagnostics

Luo and Stephens [2006] examined SPCAM simulations and suggested that a large convection-wind-evaporation feedback, partially caused by the two-dimensional geometry of the embedded CRMs in the global model, could cause the positive surface rainfall bias. *Kim et al.* [2011] examined the relationships between intraseasonal variability (ISV) and precipitation bias in atmospheric GCMs. They also found that evaporation is larger in the stronger ISV models than in the weak ones. This result is consistent with the feedback suggested by *Luo and Stephens* [2006]. However, they also found this feedback occurs in models with cumulus parameterization. They suggested that other physical processes (i.e., air-sea interaction using ocean models) might cause this positive precipitation bias.

Table 5 shows the evaporation rate (or latent heat flux) in mm d^{-1} from the four GMMF experiments. It also shows the surface rainfall rate for comparison. The observed precipitation rate, the evaporation rate over ocean, and the evaporation rate over land come from GPCP, OAFlux (Objectively Analyzed air-sea Fluxes; *Yu and Weller* [2007]), and FLUXNET [*Baldocchi et al.*, 2001], respectively. The OAFlux project uses objective analysis to synthesize measurements/estimates from various sources and provides surface fluxes and flux-related surface meteorology globally for ice-free oceans. FLUXNET is a gridded flux product from a global network of more than 500 micrometeorological tower sites. This gridded product is useful for model validation from local to global scales [*Jung et al.*, 2009; *Blyth et al.*, 2010]. All GMMF simulations in general overestimate surface precipitation and evaporation rates over ocean but underestimate them over land. The results show that a higher evaporation rate is associated with more surface rainfall over oceans. For example, the M32 and M64 runs show more surface rainfall and higher surface evaporation rates than those for the M128 and 256 runs. The surface evaporation rate is much lower over the deep Tropics (15°S to 15°N) for the M128 and M256 runs than for the M32 and M64. On the other hand, more surface rainfall over land in the M128 and M256 runs corresponds to more evaporation over land. However, the differences between the M32 and M64 runs and the M128 and M256 runs are smaller over land than they are over ocean.

Figure 7 shows mean surface evaporation (in mm d^{-1} for comparison with the surface rainfall) for the M32, M64, M128, and M256 simulations as well as for the combination of the OAFlux and FLUXNET products for comparison. The results show a very similar spatial distribution for all four GMMF runs. Peak evaporation is larger in the M32 simulation than in the other three runs. These regional maxima are smaller in the M256 run than those in the M64 and M128 runs. In terms of the zonal mean evaporation bias (Figure 7f), the M32 simulation clearly has a higher evaporation bias from 15°S to 15°N than the other simulations. It is worth noting that the areas of largest surface evaporation are not colocated with the areas of highest surface rainfall (Figure 4). For example, the areas of large surface evaporation are located well south and well north of the ITCZ and West Atlantic. Also, large surface evaporation occurs south of the large surface rainfall over the Indian Ocean. This suggests that local surface latent heat flux is not a major physical process with regard to the precipitation bias.

Low-level water vapor flux convergence, which is the integral of water vapor flux convergence from the surface to 700 hPa, was calculated from the flux form of the moisture

equation to examine its relation to surface rainfall (Figure 8). The results show that all of the simulations have very similar spatial patterns that are also similar to their surface rainfall patterns. Large values of water vapor flux convergence are colocated with the large surface rainfall regions. For example, strong water vapor flux convergence occurs over the ITCZ, SPCZ, Indian Ocean and West Atlantic where the larger rainfall occurs (see Figure 5). In addition, low-level water vapor flux convergence over land (South America and Africa) also coincides with areas of large surface rainfall. The results indicate that there is a close relationship between low-level water vapor flux convergence and surface rainfall. Figure 8 also shows that the M32 (M256) simulation has the largest (smallest) low-level water vapor flux convergence among all four runs. Low-level water vapor flux convergence is mainly controlled by the large-scale circulation.

Dynamic processes are also therefore examined to explain the differences between these runs. Figure 9 shows annual average, zonal mean meridional mass stream function values, and mean vertical pressure velocity from the M32 and M256 simulations. The meridional mass stream function, Ψ, is expressed as

$$\Psi = \frac{2\pi\cos(\varphi)}{g}\int_{p}^{PS} v dp,$$

where a is the Earth's radius, g is the gravitational acceleration, φ is the latitude, P_s is the surface pressure, p is the pressure, and v is the zonal average meridional wind. The stream function values are assumed to be zero at the top and bottom boundaries to ensure mass conservation and a steady state solution to the continuity equation. Positive and negative stream function values represent counterclockwise and clockwise circulations, respectively, and their amplitude measures the strength of the circulation. The M32 and M256 average stream functions (Figure 9) both show a roughly symmetric two-cell structure with a mutual ascending branch located north (~5°N) of the equator. The minimum/maximum values of mass stream function are −11.92/10.39 ($\times 10^{10}$ kg s^{-1}) and −11.25/9.10 ($\times 10^{10}$ kg s^{-1}) for the M32 and M256 simulations, respectively. These results indicate that the strength of both the southern and northern Hadley circulations in the M32 run is stronger than those in the M256. A stronger Hadley circulation in M32 allows for stronger low-level water vapor flux transport from the subtropics to the Tropics as shown in Figure 8.

The vertical velocity is clearly much stronger in the M32 simulation than in the M256 with M64 and M128 in between for both tropical ocean and land regions (Figures 10a and 10b). There is a larger difference over ocean than over land. These results are consistent with the rainfall (Figure 4 and Table 5) with the M32 simulation having more surface rainfall than the M256. Figure 10 also shows the vertical velocity in the subtropics over ocean and land. There is stronger subsidence in the M32 run than in the M256 with M64 and M128 again in between for both land and ocean, which is consistent with the subtropical surface rainfall patterns as well. These results also suggest that the stronger subsidence in the subtropics could allow more warming and drying in the M32 run and consequently more surface fluxes (i.e., evaporation).

Donner et al. [2001] examined the impact of mesoscale effects in an atmospheric GCM. They incorporated both convective-scale vertical velocity and mesoscale effects into a cumulus parameterization scheme based on mass fluxes and found that the results were in better agreement with satellite observations (i.e., TRMM and NVAP—the NASA Water Vapor Project) if both convective and mesoscale effects are included. Their results also indicated that mass fluxes are smaller when the mesoscale component is included. This is in good agreement with our current results. *Donner et al*. [2001] did not discuss the mesoscale effects on surface rainfall.

The impact of mesoscale precipitation systems within global circulation models has been examined. For example, *Schumacher et al*. [2004] studied the tropical dynamic response to latent heating estimates derived from the TRMM precipitation radar within an idealized simulation. Their results showed that stratiform fraction plays an important role in shaping the structure of the large-scale tropical circulation response to precipitating cloud systems. Cold pools (typically associated with convective systems) were considered in *Del Genio et al*. [2015] and do have an impact on the MJO simulations (but entrainment from convection can determine whether or not a realistic MJO can be simulated). But, they have more impact on upper-level cloudiness, which interacts with radiative heating [*Del Genio et al*., 2015]. Their model simulations were 30 days long.

3.4. Sensitivity to Reduced Evaporative Fluxes

Kim et al. [2011] have examined the relationship between intraseasonal variability and mean state bias in several GCMs as well as the relationship between surface evaporative fluxes and precipitation. Their results showed a positive correlation between evaporative fluxes and precipitation. The models with more evaporative fluxes simulated more precipitation. They suggested that the over-estimated surface rainfall in GCMs is likely due to the prescribed SST lower boundary.

To examine the role of air-sea interaction within climate simulation, *Stan et al*. [2010] coupled the SPCAM to a full-physics ocean model, POP (the Parallel Ocean Program). They found the coupled model eliminated excessive precipitation over the western Pacific during summer and produced a better simulation of the Asian monsoon circulation than the uncoupled SPCAM. However, this improved simulation could also be due to the fact that the SSTs could deviate from observations in the coupled model. *Stan et al*. [2010] also showed there were mean SST cold biases of 1–2 K with an RMSE value of 2 K [*Randall et al*., 2016] in many locations. These cold biases must have a large impact on the simulated surface evaporation, precipitation, and circulation patterns. To provide a more realistic air-sea interaction, *Benedict and Randall* [2011] coupled the SPCAM to a simplified slab ocean model that was constrained to observed climatology. Although the annual mean SST variations were only a few tenths of a degree from the observed SSTs, they found the organization and eastward propagation of the MJO to be more realistic than in the uncoupled SPCAM. However, the excessive annual mean precipitation in the tropics and western Pacific still existed.

To investigate the impact of SST cold biases of 1–2 K on surface evaporation, precipitation pattern, and the Hadley circulation, a simple sensitivity test was conducted using the M32

configuration but with the SSTs reduced (in °C) by 5%. Surface evaporation is reduced compared to the control (M32) run (Figures 11a and 7b), lowering both the bias and RMSE (bias from 0.477 to 0.319; RMSE from 1.017 to 0.782), while increasing the correlation from 0.816 to 0.937. These statistics are quite comparable to the M256 simulation (i.e., a 0.345 bias, an RMSE of 0.781, and a 0.939 correlation). Nevertheless, the spatial distribution between this run and the M32 run is quite similar. As surface evaporation is reduced, surface rainfall is also reduced compared to the M32 run (Figure 11b and Figure 4c) in better agreement with observations. The bias/RMSE/CORR for precipitation against GPCP observations is 0.131/1.563/0.816 for the reduced SST scenario. The results are again quite similar to those for the M256 simulation (see Table 4). The zonal meridional mass stream function (Figure 11d) has minimum/maximum values of −12.99/9.79 ($\times 10^{10}$ kg s^{-1}), which are smaller than those [−11.92/10.39 ($\times 10^{10}$ kg s^{-1})] for the M32 experiment (Figure 9a). This demonstrates that the southern (northern) branch of the Hadley circulation is stronger (weaker) in the sensitivity test versus the control. The reduction of tropical precipitation in the SST-5% experiment is associated with smaller low-level moisture flux convergence (Figure 11c). This can be attributed mainly to a drier lower atmosphere as a result of weaker surface latent heat fluxes in the SST-5% sensitivity experiment. These results show that the SST cold biases in a coupled model could have a significant influence on the large-scale circulation and precipitation distributions through convection-wind-evaporation feedback [*Luo and Stephens*, 2006] in a superparameterization model system.

4. Summary and Conclusions

Almost all MMFs (including the GMMF) have used 32 or 64 grid points with 4 km grid spacing in their embedded CRMs and overestimated precipitation (surface rainfall) in the Tropics. In this study, the major physical processes are examined and identified that cause the overestimated rainfall in the GMMF. Both GCE and GMMF simulations are conducted with different numbers of CRM grid points and spacing. In addition, a sensitivity test with the GMMF using reduced SSTs was conducted. The main results from this modeling study are as follows:

1. Overall, the GCE setup with the most grid points (i.e., C256 case) and highest resolution (1 km) has the lowest bias and highest correlation in terms of surface rainfall. In contrast, the GCE setup with the fewest grid points (i.e., the C32 configuration) and lower resolution (4 km) has the lowest correlation with surface rainfall. The other two simulations (i.e., C64 and C128) have biases and correlations in between the C256 and C32 runs.
2. The GCE setup with more grid points (C256) produces more long-lived, organized convective systems and a temporal rainfall variation in very good agreement with observations. This result is in good agreement with previous CRM simulations that a larger domain is required to better simulate organized convection [i.e., *Johnson et al.*, 2002; *Tompkins*, 2000; *Petch and Gray*, 2001].
3. The GCE configuration with the least grid points (C32) simulates short-lived, isolated convection. Its simulated domain-mean rainfall also lasts for a shorter time period and is stronger compared to the other runs and to observations.

4. Overall, the GMMF simulations show very similar surface rainfall patterns and capture the major weather phenomena, such as a single ITCZ and SPCZ and large rainfall over the Indian Ocean, South America, and Eastern Atlantic. However, all of the GMMF simulations over-estimated the total rainfall amount compared to satellite estimates from TRMM and GPCP.

5. However, the GMMF with more CRM grid points and higher resolution (M256) has a lower bias, smaller RMSE and higher correlation versus surface rainfall compared to those with fewer grid points and lower resolution (i.e., M32, M64, and M128). Overall, the M256 and M128 simulations are in better agreement with observations than the M32 and M64.

6. The M256 simulation produced more organized convective systems than the M32 and M64 with the M32 setup resulting in more isolated convection. These GMMF results are consistent with the GCE model (noncoupled) simulations.

7. The GMMF simulations indicate that convection-wind-evaporation feedback is a key process for tropical precipitation. Globally, more (less) surface evaporation produces more (less) surface rainfall. This result is in good agreement with previous model results [*Luo and Stephens*, 2006; *Kim et al.*, 2001]. However, maximum surface evaporation occurs in subtropical regions. It is the large-scale low-level circulation that transports the moisture from the subtropics to the tropical ITCZs and SPCZ where the heavy rainfall occurs.

8. The mean vertical velocity in the tropical region is weaker (stronger) for the M256 (M32) configuration. This is consistent with the results of *Donner et al.* [2001] wherein mass fluxes are stronger when the mesoscale effect is not considered in the cumulus parameterization.

9. The stronger upward motion in the Tropics can allow stronger subsidence in the subtropics. The warm, dry air associated with the subsidence that can then allow larger surface evaporation.

10. The upward motion in the Tropics also affects the Hadley circulation. A stronger (weaker) Hadley circulation allows more (less) large-scale low-level water vapor to be transported from the subtropics to the Tropics.

11. Surface evaporation is weaker in the GMMF sensitivity test wherein SSTs were reduced by 5% compared to the control simulation (M32). Consequently, the tropical rainfall is also reduced due to smaller low-level moisture flux convergence associated with a drier low atmosphere. These results suggest that the cold SST biases in a coupled model can play an important role in the global rainfall distribution.

One of the key findings in this paper is that MCSs can be simulated in both the stand-alone GCE and the embedded GCEs in the GMMF. But, it requires a relatively large number of CRM grid points. For example, the GMMF M256 simulation needs much more computation resources compared to the M32. Its computational requirement is similar to a GCRM at ~10 km grid spacing. The next step would be to compare the performance of the M256

configuration with the 7 km GEOS5 model (most of GCRMs do not use 1 km grids, but more typically 3.5, 7, and 14 km).

One of the major limitations of MMFs is the use of a 2-D CRM with cyclic lateral boundary conditions. Another limitation is that the MMF-embedded CRM zonal momentum is usually nudged to the large-scale model's momentum. Both could directly affect the large-scale organization of convection [*Moncrieff*, 2004]. For example, only one type of MCS (squall line) can be simulated by a 2-D CRM. In addition, horizontal momentum could be counter-gradient for some types of convective organization [*LeMone et al.*, 1984; *Soong and Tao*, 1984; *Moncrieff*, 2004]. Only two recent MMFs [*Tulich*, 2015; *Cheng and Xu*, 2014] have considered the convective momentum transport (CMT). Both approaches utilize the low-level (surface to 4 km level) GCM wind shear to determine the orientation of the 2-D CRM. For example, the orientation of the CRM can be perpendicular to the shear for organized (deep) convection or parallel to it for shallow clouds. However, the GCM resolution is quite coarse and the low-level wind shear may not be a good indicator of the convective organization. Nevertheless, the inclusion of CMT does improve the horizontal distribution of surface rainfall but not its total amount (see Figure 16 in *Tulich* [2015] and Figure 1 *Cheng and Xu* [2014]). This topic is an on-going area of research and is beyond the scope of this paper.

Acknowledgments

The GCE and GMMF models are mainly supported by the NASA Precipitation Measurement Mission (PMM) and the NASA Modeling, Analysis, and Prediction (MAP) Program, respectively. The authors are grateful to Ramesh Kakar and David B. Considine at NASA headquarters for their support of this research and to Stephen Lang for carefully proofing the manuscript. We also thank M. Moncrieff and two anonymous reviewers for their constructive comments that improved this paper significantly. Acknowledgment is also made to the NASA Goddard Space Flight Center and NASA Ames Research Center computing facilities and to Tsengdar Lee at NASA HQ for the computational resources used in this research. The results shown in section 3.1 were mainly produced by Sung-Yoon Kim and Myong-In Lee at the School of Urban and Environmental Engineering, Ulsan National Institute of Science & Technology (UNIST), Republic of Korea. The model outputs used in this study are available upon request from weikuo.tao-1@nasa.gov. The GPCP and TRMM data sets used in this study are accessible from http://precip.gsfc.nasa.gov.

References

Adler RF, et al. (2003), The version 2 Global Precipitation Climatology Project (GPCP) monthly precipitation analysis (1979-present), J. Hydrometeorol, 4, 1147–1167, doi:10.1175/1525-7541(2003)004<1147:TVGPCP>2.0.CO;2.

Baldocchi D, et al. (2001), FLUXNET: A new tool to study the temporal and spatial variability of ecosystem-scale carbon dioxide, water vapor, and energy flux densities, Bull. Am. Meteorol. Soc, 82, 2415–2434.

Benedict JJ, and Randall DA (2009), Structure of the Madden-Julian oscillation in the superparameterized CAM, J. Atmos. Sci, 66, 3277–3296, doi:10.1175/2009JAS3030.1.

Benedict JJ, and Randall DA (2011), Impacts of idealized air-sea coupling on Madden-Julian oscillation structure in the superparameterized CAM, J. Atmos. Sci, 68, 1990–2008, doi:10.1175/JAS-D-11-04.1.

Blyth E, Gash J, Lloyd A, Pryor M, Weedon GP, and Shuttleworth J (2010), Evaluating the JULES land surface model energy fluxes usingFLUXNET data, J. Hydrometeorol, 11, 509–519, doi:10.1175/2009JHM1183.1.

Cheng A, and Xu K-M (2011), Improved low-cloud simulation from a multiscale modeling framework with a third-order turbulence closure in its cloud-resolving model component, J. Geophys. Res, 116, D14101, doi:10.1029/2010JD015362.

Cheng A, and Xu K-M (2014), An explicit representation of vertical momentum transport in a multiscale modeling framework through its 2-D cloud-resolving model component, J. Geophys. Res. Atmos, 119, 2356–2374, doi:10.1002/2013JD021078.

Chern J-D, Tao W-K, Lang SE, Matsui T, Li J-LF, Mohr KI, Skofronick-Jackson GM, and Peters-Lidard CD (2016), Performance of the Goddard multiscale modeling framework with Goddard ice microphysical schemes, J. Adv. Model. Earth Syst, 8, 66–95, doi:10.1002/2015MS000469.

Cotton W, Alexander GD, Hertenstein R, Walko RL, McAnelly RL, and Nicholls M (1995), Cloud venting: A review and some new global annual estimates, Earth Sci. Rev, 39, 169–206.

Dee DP, et al. (2011), The ERA-Interim reanalysis: Configuration and performance of the data assimilation system, Q. J. R. Meteorol. Soc, 137, 553–597, doi:10.1002/qj.828.

Del Genio AD, Wu J, Wolf AB, Chen Y, Yao M-S, and Kim D (2015), Constraints on cumulus parameterization from simulations of observed MJO events, J. Clim, 28, 6419–6442, doi:10.1175/JCLI-D-14-00832.1.

DeMott CA, Randall DA, and Khairoutdinov M (2007), Convective precipitation variability as a tool for general circulation model analysis, J. Clim, 20, 91–112, doi:10.1175/JCLI3991.1.

DeMott CA, Randall DA, and Khairoutdinov M (2010), Implied ocean heat transports in the standard and superparameterized Community Atmospheric Models, J. Clim, 23, 1908–1928. doi:10.1175/2009JCLI2987.1.

DeMott CA, Stan C, Randall DA, Kinter III JL, and Khairoutdinov M (2011), The Asian monsoon in the super-parameterized CCSM and its relationship to tropical wave activity, J. Clim, 24, 5134–5156, doi:10.1175/2011JCLI4202.1.

DeMott CA, Stan C, and Randall DA (2013), Northward propagation mechanisms of the boreal summer intraseasonal oscillation in theERA-Interim and SP-CCSM, J. Clim, 26, 1973–1992, doi:10.1175/JCLI-D-12-00191.1.

Dirmeyer PA, et al. (2012), Simulating the diurnal cycle of rainfall in global climate models: Resolution versus parameterization, Clim. Dyn, 39, 399–418, doi:10.1007/s00382-011-1127-9.

Donner LJ, Seman CJ, Hemler RS, and Fan S (2001), A cumulus parameterization including mass fluxes, convective vertical velocities, and mesoscale effects: Thermodynamic and hydrological aspects in a general circulation model, J. Clim, 14, 3444–3463.

Goswami BB, Mani NJ, Mukhopadhyay P, Waliser DE, Benedict JJ, Maloney ED, Khairoutdinov M, and Goswami BN (2011), Monsoon intraseasonal oscillations as simulated by the superparameterized Community Atmosphere Model, J. Geophys. Res, 116, D22104, doi:10.1029/2011JD015948.

Goswami BB, Mukhopadhyay P, Khairoutdinov M, and Goswami BN (2013), Simulation of Indian summer monsoon intraseasonal oscillations in a superparameterized coupled climate model: Need to improve the embedded cloud resolving model, Clim. Dyn, 41, 1497–1507, doi:10.1007/s00382-012-1563-1.

Grabowski WW, and Smolarkiewicz PK (1999), CRCP: A Cloud Resolving Convection Parameterization for modeling the tropical convecting atmosphere, Physica D, 133, 171–178.

Houze RA Jr. (1982), Cloud clusters and large-scale vertical motions in the tropics, J. Meteorol. Soc. Jpn, 60, 396–409.

Houze RA Jr. (1989), Observed structure of mesoscale convective systems and implications for large-scale heating, Q. J. R. Meteorol. Soc, 115, 425–461.

Huffman GJ, et al. (2007), The TRMM Multi-satellite Precipitation Analysis: Quasi-global, multi-year, combined-sensor precipitation estimates at fine scale, J. Hydrometeorol, 8, 38–55, doi:10.1175/JHM560.1.

Huffman GJ, Adler RF, Bolvin DT, and Nelkin EJ (2010), The TRMM Multi-satellite Precipitation Analysis (TMPA), in Satellite Rainfall Applications for Surface Hydrology, edited by Hossain F and Gebremichael M, pp. 3–22, Springer, Dordrecht, Netherlands, ISBN: 978-90-481-2914-0.

Johnson DE, Tao W-K, Simpson J, and Sui C-H (2002), A study of the response of deep tropical clouds to large-scale thermodynamic forcings, Part I: Modeling strategies and simulations of TOGA COARE convective systems, J. Atmos. Sci, 59, 3492–3518.

Jung M, Reichstein M, and Bondeau A (2009), Towards global empirical upscaling of FLUXNET eddy covariance observations: Validation of a model tree ensemble approach using a biosphere model, Biogeosciences, 6, 2001–2013.

Khairoutdinov MF, and Randall DA (2001), A cloud resolving model as a cloud parameterization in the NCAR Community Climate System Model: Preliminary results, Geophys. Res. Lett, 28, 3617–3620.

Khairoutdinov MF, and Randall DA (2003), Cloud resolving modeling of the ARM summer 1997 IOP: Model formulation, results, uncertainties, and sensitivities, J. Atmos. Sci, 60, 607–625, doi:10.1175/1520-0469(2003)060<0607:CRMOTA>2.0.CO;2.

Khairoutdinov M, Randall D, and DeMott C (2005), Simulations of the atmospheric general circulation using a cloud-resolving model as a superparameterization of physical processes, J. Atmos. Sci, 62, 2136–2154, doi:10.1175/JAS3453.1.

Khairoutdinov M, DeMott C, and Randall D (2008), Evaluation of the simulated interannual and subseasonal variability in an AMIP-style simulation using the CSU Multiscale Modeling Framework, J. Clim, 21, 413–431, doi:10.1175/2007JCLI1630.1.

Kidd C, Matsui T, Chern J-D, Mohr KI, Kummerow C, and Randel D (2016), Global precipitation estimates from cross-track passive microwave observations using a physically based retrieval scheme, J. Hydrometeorol, 17, 383–400, doi:10.1175/JHM-D-15-0051.1.

Kim D, Sobel AH, Maloney ED, Frierson DMW, and Kang IS (2011), A systematic relationship between intraseasonal variability and mean state bias in AGCM simulations, J. Clim, 24, 5506–5520, doi:10.1175/2011JCLI4177.1.

Kodama C, et al. (2015), A 20-Year climatology of a NICAM AMIP-type simulation, J. Meteorol. Soc. Jpn, 93, 393–424, doi:10.2151/jmsj.2015-024.

Kooperman GJ, Pritchard MS, Ghan SJ, Wang M, Somerville RCJ, and Russell LM (2012), Constraining the influence of natural variability to improve estimates of global aerosol indirect effects in a nudged version of the Community Atmosphere Model 5, J. Geophys. Res, 117, D23204, doi:10.1029/2012JD018588.

Lang S, Tao W-K, Simpson J, and Ferrier B (2003), Modeling of convective-stratiform precipitation processes: Sensitivity to partitioning methods, J. Appl. Meteorol, 42, 505–527, doi:10.1175/1520-0450(2003)042<0505:MOCSPP>2.0.CO;2.

Lang S, Tao W-K, Chern J-D, Wu D, and Li X (2014), Benefits of a 4^{th} ice class in the simulated radar reflectivities of convective systems using a bulk microphysics scheme, J. Atmos. Sci, 71, 3583–3612, doi:10.1175/JAS-D-13-0330.1.

Legates DR, and Willmott CJ (1990), Mean seasonal and spatial variability in global surface air temperature, Theor. Appl. Climatol, 41, 11–21, doi:10.1007/BF00866198.

LeMone MA, Barnes GM, and Zipser EJ (1984), Momentum flux by lines of cumulonimbus over the tropical oceans, J. Atmos. Sci, 41(12), 1914–1932, doi:10.1175/1520-0469(1984)041<1914:MFBLOC>2.0.CO;2.

Li F, Rosa D, Collins WD, and Wehner MF (2012), “Super-parameterization”: A better way to simulate regional extreme precipitation?, J. Adv. Model. Earth Syst, 4, M04002, doi:10.1029/2011MS000106.

Luo Z, and Stephens GL (2006), An enhanced convection-wind-evaporation feedback in a superparameterization GCM (SP-GCM) depiction of the Asian summer monsoon, Geophys. Res. Lett, 33, L06707, doi:10.1029/2005GL025060.

Marchand R, and Ackerman T (2010), An analysis of cloud cover in multiscale modeling framework global climate model simulations using 4 and 1 km horizontal grids, J. Geophys. Res, 115, D16207, doi:10.1029/2009JD013423.

Marchand R, Haynes J, Mace GG, Ackerman T, and Stephens G (2009), A comparison of simulated cloud radar output from the multi-scale modeling framework global climate model with CloudSat cloud radar observations, J. Geophys. Res, 114, D00A20, doi:10.1029/2008JD009790.

Matsui T, Chern J-D, Tao W-K, Lang S, Satoh M, Hashino T, and Kubota T, (2016), On the land-ocean contrast of tropical convection and microphysics statistics derived from TRMM satellite signals and global storm-resolving models. J. Hydrometeorol, 17, 1425–1445, doi:10.1175/JHM-D-15-0111.1. [PubMed: 32818023]

Miyamoto Y, Kajikawa Y, Yoshida R, Yamaura T, Yashiro H, and Tomita H (2013), Deep moist atmospheric convection in a subkilometer global simulation, Geophys. Res. Lett, 40, 4922–4926, doi:10.1002/grl.50944.

Mohr KI, Tao W-K, Chern J-D, Kumar SV, and Peters-Lidard CD (2013), The NASA-Goddard Multi-scale Modeling Framework-Land Information System: Global land/atmosphere interaction with resolved convection, Environ. Modell. Software, 39, 103–115, doi:10.1016/j.envsoft.2012.02.023.

Moncrieff MW (2004), Analytic representation of the large-scale organization of tropical convection, J. Atmos. Sci, 61, 1521–1538.

Nesbitt SW, Cifelli R, and Rutledge SA (2006), Storm morphology and rainfall characteristics of TRMM precipitation features, Mon. Weather Rev, 134, 2702–2721.

Ooyama KV (2001), A dynamic and thermodynamic foundation for modeling the moist atmosphere with parameterized microphysics, J. Atmos. Sci, 58, 2073–2102, doi:10.1175/1520-0469(2001)058<2073:ADATFF>2.0.CO;2.

Ovtchinnikov M, Ackerman T, Marchand R, and Khairoutdinov M (2006), Evaluation of the multiscale modeling framework using data from the Atmospheric Radiation Measurement Program, J. Clim, 19, 1716–1729.

Petch JC, and Gray MEB (2001), Sensitivity studies using a cloud-resolving model simulation of the tropical west Pacific, Q. J. R. Meteorol. Soc, 127, 2287–2306.

Pritchard MS, and Somerville RCJ (2009), Assessing the diurnal cycle of precipitation in a multi-scale climate model, J. Adv. Model. Earth Syst, 1, 12, doi:10.3894/JAMES.2009.1.12.

Pritchard MS, and Bretherton CS (2014), Causal evidence that rotational moisture advection is critical to the superparameterized Madden-Julian oscillation, J. Atmos. Sci, 71, 800–815, doi:10.1175/JAS-D-13-0119.1.

Pritchard MS, Moncrieff MW, and Somerville RCJ (2011), Orogenic propagating precipitation systems over the United States in a global climate model with embedded explicit convection, J. Atmos. Sci, 68, 1821–1840, doi:10.1175/2011JAS3699.1.

Pritchard MS, Bretherton CS, and DeMott CA (2014), Restricting 32–128 km horizontal scales hardly affects the MJO in the Superparameterized Community Atmosphere Model v.3.0 but the number of cloud-resolving grid columns constrains vertical mixing, J. Adv. Model. Earth Syst, 6, 723–739, doi:10.1002/2014MS000340.

Putman WM, and Suarez M (2011), Cloud-system resolving simulations with the NASA Goddard Earth Observing System global atmospheric model (GEOS-5), Geophys. Res. Lett, 38, L16809, doi:10.1029/2011GL048438.

Randall DA, Khairoutdinov M, Arakawa A, and Grabowski W (2003), Breaking the cloud parameterization deadlock, Bull. Am. Meteorol. Soc, 84, 1547–1564.

Randall D, DeMott C, Stan C, Khairoutdinov M, Benedict J, McCrary R, Thayer-Calder K, and Branson M (2016), Simulations of the tropical general circulation with a multiscale global model, Meteorol. Monogr, 56, 15.1–15.15, doi:10.1175/AMSMONOGRAPHS-D-15-0016.1.

Reynolds RW, et al. (2007), Daily high-resolution-blended analyses for sea surface temperature, J. Clim, 20, 5473–5496, doi:10.1175/2007JCLI1824.1.

Rosa D, and Collins WD (2013), A case study of subdaily simulated and observed continental convective precipitation: CMIP5 and multi-scale global climate models comparison, Geophys. Res. Lett, 40, 5999–6003, doi:10.1002/2013GL057987.

Rosa D, Lamarque JF, and Collins WD (2012), Global transport of passive tracers in conventional and superparameterized climate models: Evaluation of multi-scale methods, J. Adv. Model. Earth Syst, 4, M10003, doi:10.1029/2012MS000206.

Satoh M, Tomita H, Miura H, Iga S, and Nasuno T (2005), Development of a global cloud resolving model—A multi-scale structure of tropical convections, J. Earth Simul, 3, 11–19.

Satoh M, et al. (2008), Nonhydrostatic Icosahedral Atmospheric Model (NICAM) for global cloud resolving simulations, J. Comput. Phys, 227, 3486–3514, doi:10.1016/j.jcp.2007.02.006.

Satoh M, et al. (2014), The Non-hydrostatic Icosahedral Atmospheric Model: Description and development, Prog. Earth Planet. Sci, 1, 18, doi:10.1186/s40645-014-0018-1.

Schumacher C, Houze RA, and Kraucunas I (2004), The tropical dynamical response to latent heating estimates derived from the TRMM precipitation radar, J. Atmos. Sci, 61, 1341–1358.

Skamarock WC, Park S-H, Klemp JB, and Snyder C (2014), Atmospheric kinetic energy spectra from global high-resolution nonhydrostatic simulations, J. Atmos. Sci, 71, 4369–4381, doi:10.1175/JAS-D-14-0114.1.

Simpson J, Kummerow C, Tao W-K, and Adler RF (1996), On the Tropical Rainfall Measuring Mission (TRMM), Meteorol. Atmos. Phys, 60, 19–36.

Soong S-T, and Tao W-K (1984), A numerical study of the vertical transport of momentum in a tropical rainband, J. Atmos. Sci, 41(6), 1049–1061, doi:10.1175/1520-0469(1984)041<1049:ANSOTV>2.0CO;2.

Stan C, and Xu L (2014), Climate simulations and projections with a super-parameterized climate model, Environ. Modell. Software, 60, 134–152, doi:10.1016/j.envsoft.2014.06.013.

Stan C, Khairoutdinov M, DeMott CA, Krishnamurthy V, Straus DM, Randall DA, Kinter III JL, and Shukla J (2010), An ocean-atmosphere climate simulation with an embedded cloud resolving model, Geophys. Res. Lett, 37, L01702, doi:10.1029/2009GL040822.

Steiner M, Houze RA Jr., and Yuter SE (1995), Climatological characteristics of three-dimensional storm structure from operational radar and rain gauge data, J. Appl. Meteorol, 34, 1978–2007.

Tao W-K, Lang SE, Simpson J, and Adler R (1993), Retrieval algorithms for estimating the vertical profiles of latent heat release: Their applications for TRMM, J. Meteorol. Soc. Jpn, 71, 685–700.

Tao W-K, et al. (2009), A multiscale modeling system: Developments, applications, and critical Issues, Bull. Am. Meteorol. Soc, 90, 515–534, doi:10.1175/2008BAMS2542.1.

Tao W-K, et al. (2014), The Goddard Cumulus Ensemble model (GCE): Improvements and applications for studying precipitation processes, Atmos. Res, 143, 392–424, doi:10.1016/j.atmosres.2014.03.005.

Tao W-K, Wu D, Lang SE, Chern J-D, Peters-Lidard CD, Fridlind A, and Matsui T (2016), High-resolution NU-WRF simulations of a deep convective-precipitation system during MC3E: Further improvements and comparisons between Goddard microphysics schemes and observations, J. Geophys. Res. Atmos, 121, 1278–1305, doi:10.1002/2015JD023986. [PubMed: 32802697]

Thayer-Calder K, and Randall DA (2009), The role of convective moistening in the Madden-Julian oscillation, J. Atmos. Sci, 66, 3297–3312, doi:10.1175/2009JAS3081.1.

Tomita H, et al. (2005), A global cloud-resolving simulation: Preliminary results from an aqua planet experiment, Geophys. Res. Lett, 32, L08805, doi:10.1029/2005GL022459.

Tompkins AM (2000), The impact of dimensionality on longterm cloud-resolving model simulations, Mon. Weather Rev, 128, 1521–1535.

Tulich SN (2015), A strategy for representing the effects of convective momentum transport in multiscale models: Evaluation using a new superparameterized version of the Weather Research and Forecast model (SP-WRF), J. Adv. Model. Earth Syst, 7, 938–962, doi:10.1002/2014MS0004617.

Wang M, Ghan S, Ovchinnikov M, Liu X, Easter R, Kassianov E, Qian Y, and Morrison H (2011), Aerosol indirect effects in a multi-scale aerosol-climate model PNNL-MMF, Atmos. Chem. Phys, 11(11), 5431–5455.

Wang M, et al. (2012), Constraining cloud lifetime effects of aerosols using A-Train satellite observations, Geophys. Res. Lett, 39, L15709, doi:10.1029/2012GL052204.

Wang M, Larson VE, Ghan S, Ovchinnikov M, Schanen DP, Xiao H, Liu X, Rasch P, and Guo Z (2015), A multiscale modeling framework model (superparameterized CAM5) with a higher-order turbulence closure: Model description and low-cloud simulations, J. Adv. Model. Earth Syst, 7, 484–509, doi:10.1002/2014MS000375.

Wyant MC, Khairoutdinov M, and Bretherton CS (2006), Climate sensitivity and cloud response of a GCM with a superparameterization, Geophys. Res. Lett, 33, L06714, doi:10.1029/2005GL025464.

Wyant MC, Bretherton CS, and Blossey PN (2009), Subtropical low cloud response to a warmer climate in a superparameterized climate model. Part I: Regime sorting and physical mechanisms, J. Adv. Model. Earth Syst, 1, 7, doi:10.3894/JAMES.2009.1.7.

Wyant MC, Bretherton CS, Blossey PN, and Khairoutdinov M (2012), Fast cloud adjustment to increasing CO_2 in a superparameterized climate model, J. Adv. Model. Earth Syst, 4, M05001, doi:10.1029/2011MS000092.

Xu KM, and Cheng A (2013a), Evaluating low cloud simulation from an upgraded Multiscale Modeling Framework model: Part I: Sensitivity to spatial resolution and climatology, J. Clim, 26, 5717–5740, doi:10.1175/JCLI-D-12-00200.1.

Xu K-M, and Cheng A (2013b), Evaluating low-cloud simulation from an upgraded Multiscale Modeling Framework model: Part II: Seasonal variations over the Eastern Pacific, J. Clim, 26, 5741–5760, doi:10.1175/JCLI-D-12-00276.1.

Yashiro H, Kajikawa Y, Miyamoto Y, Yamaura T, Yoshida R, and Tomita H (2016), Resolution dependence of the diurnal cycle of precipitation simulated by a global cloud system resolving model, SOLA, 12, 272–276, doi:10.2151/sola.2016-053.

Yoneyama K, Zhang C, and Long CN (2013), Tracking pulses of the Madden-Julian oscillation, Bull. Am. Meteorol. Soc, 94, 1871–1891, doi:10.1175/BAMS-D-12-00157.1.

Yu L, and Weller RA (2007), Objectively analyzed air-sea heat fluxes for the global ice-free oceans (1981–2005), Bull. Am. Meteorol. Soc, 88, 527–539, doi:10.1175/BAMS-88-4-527.

Zhang Y, Klein SA, Liu C, Tian B, Marchand RT, Haynes JM, Mccoy RB, Zhang Y, and Ackerman TP (2008), On the diurnal cycle of deep convection, high-level cloud, and upper troposphere water vapor in the Multiscale Modeling Framework, J. Geophys. Res, 113, D16105, doi:10.1029/2008JD009905.

Zhu H, Hendon H, and Jakob C (2009), Convection in a parameterized and superparameterized model and its role in the representation of the MJO, J. Atmos. Sci, 66, 2796–2811, doi:10.1175/2009JAS3097.1.

Key Points:

- The degree to which MCSs are resolved in multiscale modeling frameworks (MMFs) can impact their global surface rainfall amount
- Surface evaporation and the large-scale wind together determine the tropical rainfall
- An MMF with more grid points and finer resolution in its embedded CRMs can produce accurate precipitation statistics

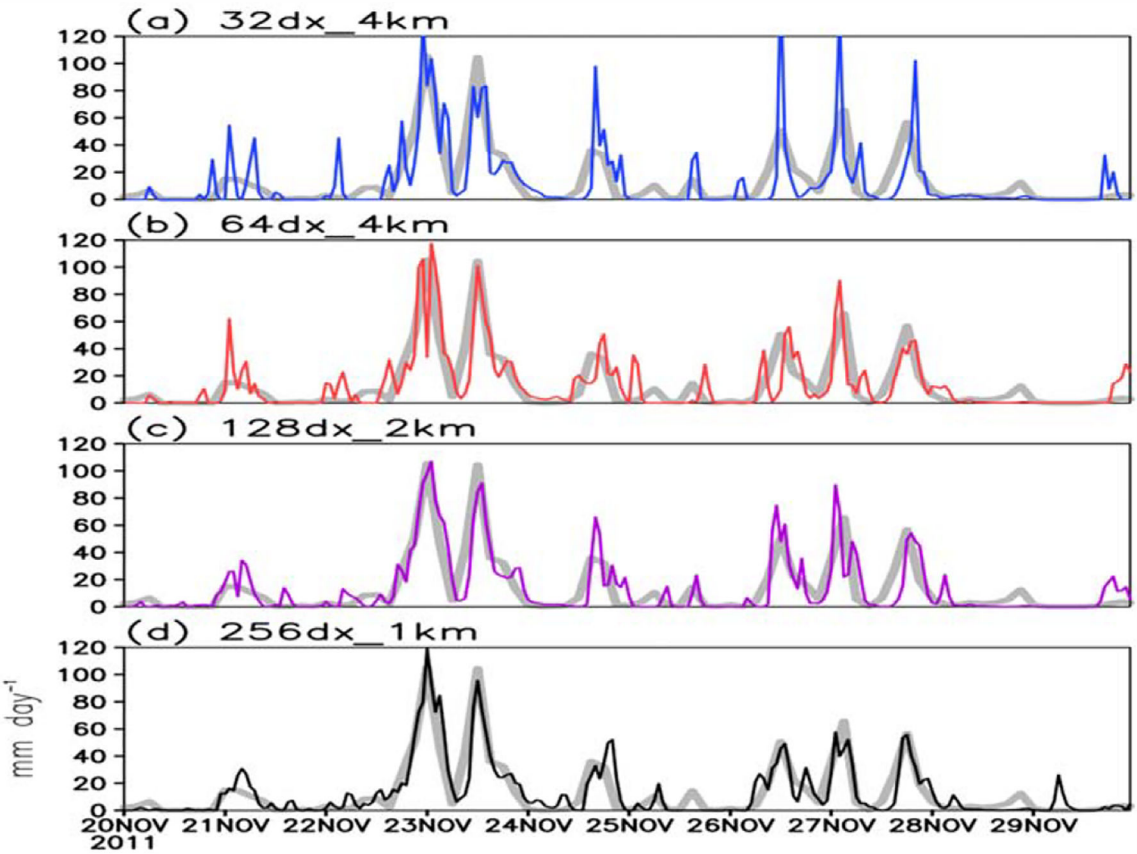

Figure 1.

Time series of GCE domain-mean surface rainfall (mm d^{-1}) for the (a) C32, (b) C64, (c) C128, and (d) C256 experiments. Thick solid lines show the observed domain-mean surface rainfall from the DYNAMO field campaign.

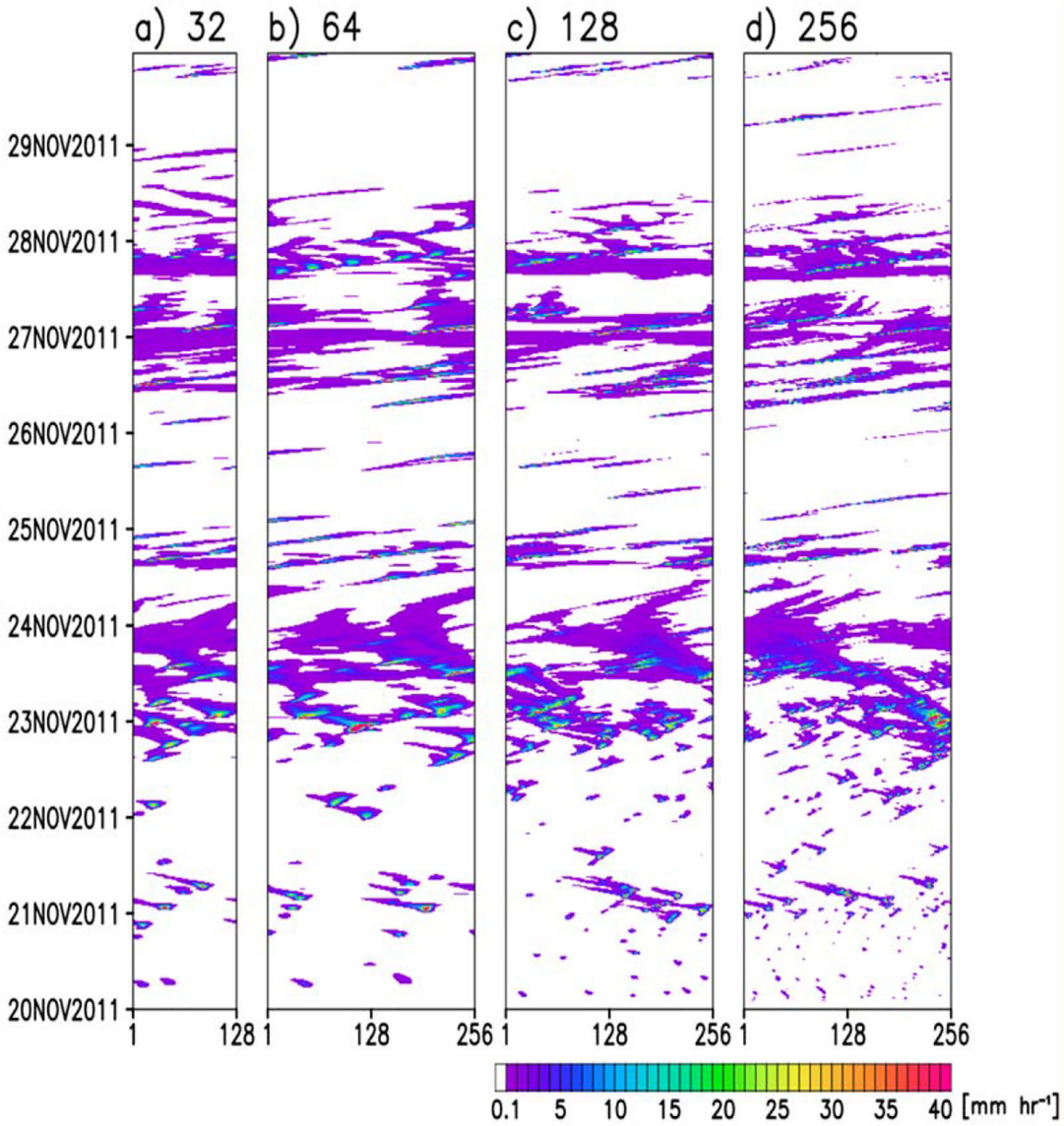

Figure 2.

Hovmoller diagrams of GCE model-simulated surface rainfall rate (mm h^{-1}) for the (a) C32, (b) C64, (c) C128, and (d) C256 experiments.

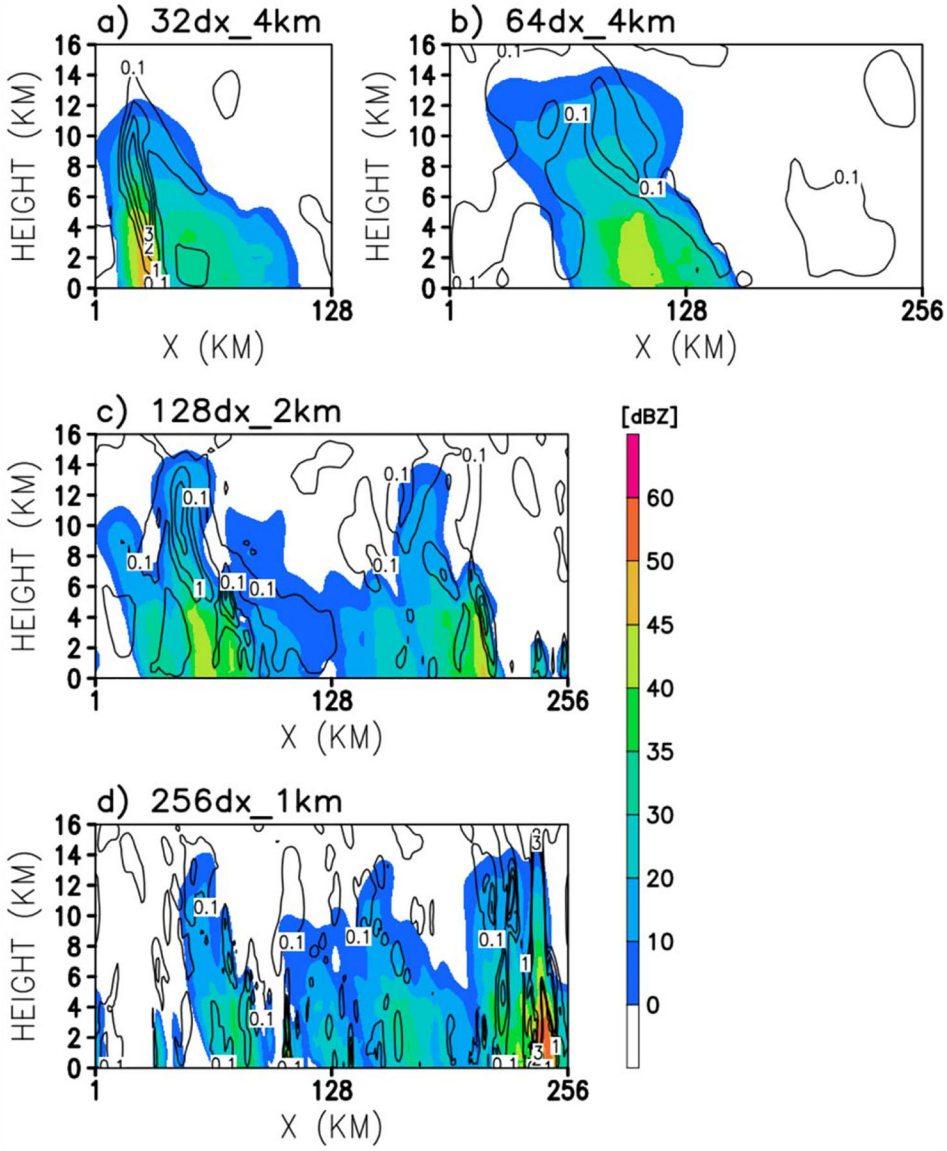

Figure 3.

CRM-simulated radar reflectivity (dBZ, color shading) and vertical velocity (m s^{-1}, contours) at 23 UTC 22 November 2011 (near the time of the peak observed rainfall) for the sensitivity runs (a) C32, (b) C64, (c) C128, and (d) C256.

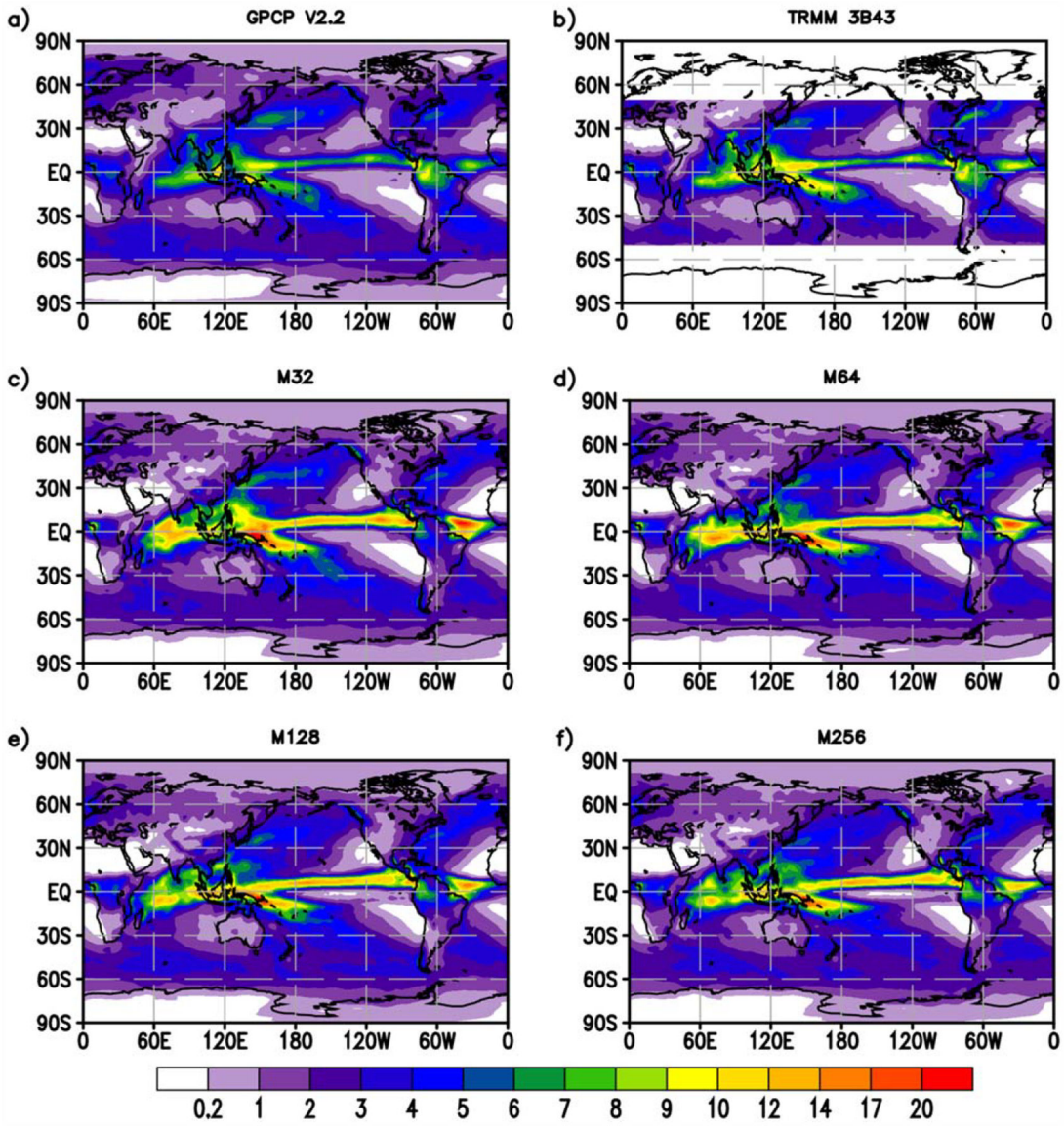

Figure 4.

Two-year (2007–2008) mean precipitation rates (mm d^{-1}) from (a) GPCP and (b) TRMM 3B43 observations and GMMF simulations for the (c) M32, (d) M64, (e) M128, and (f) M256 experiments.

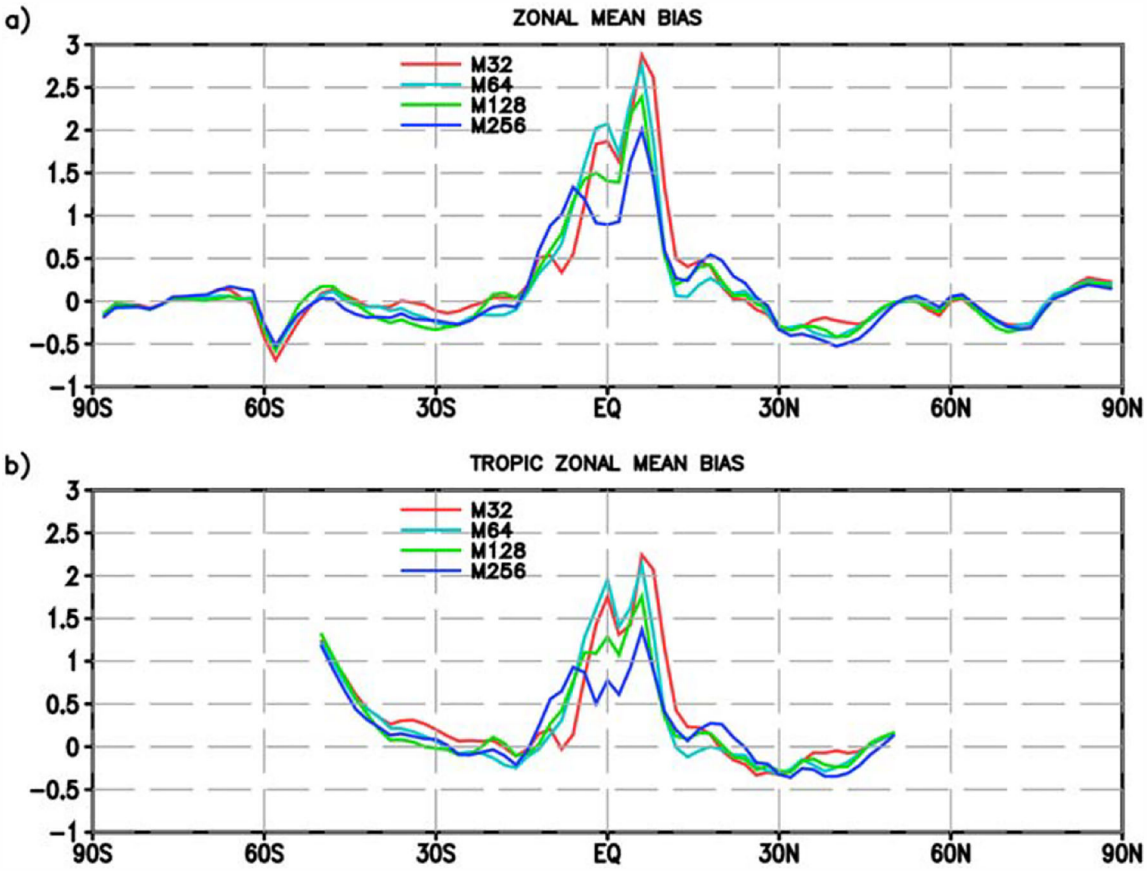

Figure 5.

GMMF mean zonal precipitation rate biases (mm d^{-1}) relative to (a) GPCP and (b) TRMM 3B43 observations. Red, light-blue, green, and dark-blue lines denote the M32, M64, M128, and M256 experiments, respectively.

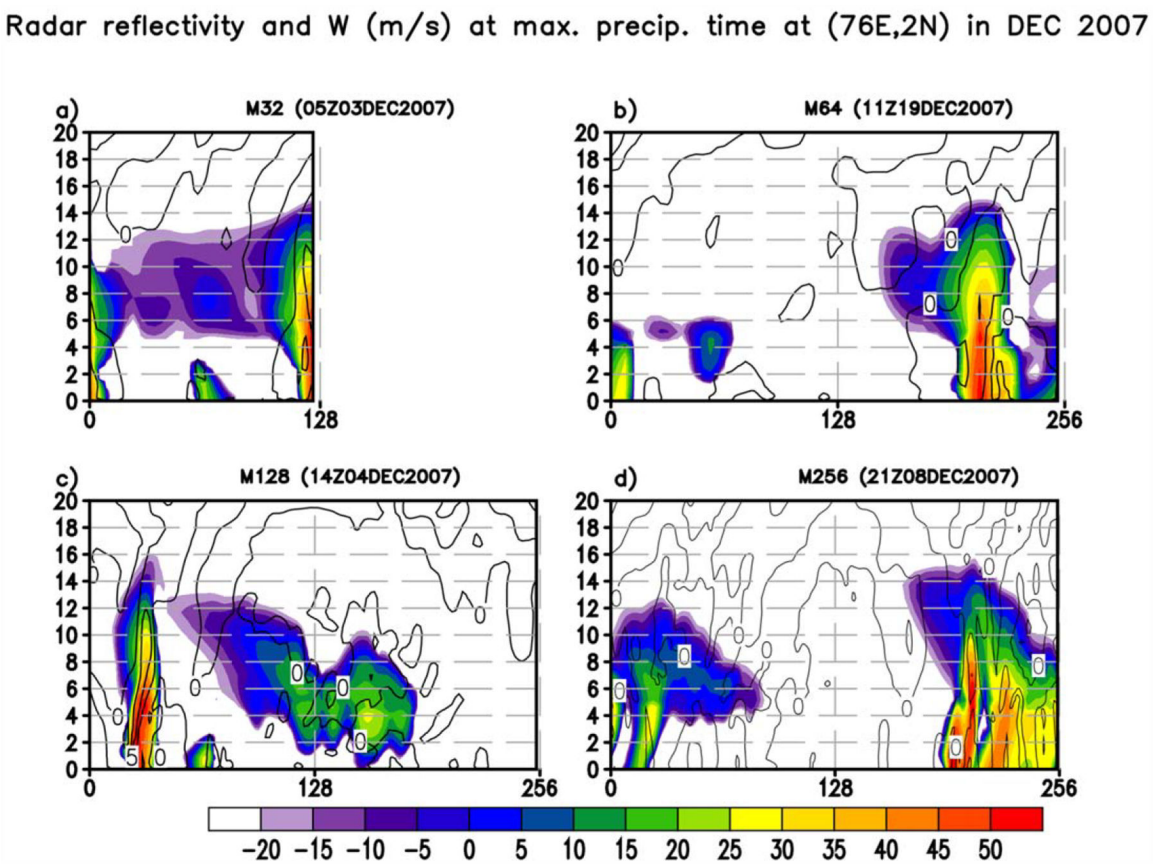

Figure 6.

GMMF-simulated radar reflectivity (dBZ, color shading) and vertical velocity (m s^{-1}, contours) at the maximum precipitation time for a GCM grid point at (76°E, 2°N), which is near the DYNAMO field campaign site (76°E, 2°N), in December 2007 for the (a) M32, (b) M64, (c) M128, and (d) M256 experiments. The MCSs/squall lines propagate westward except for the M32 case.

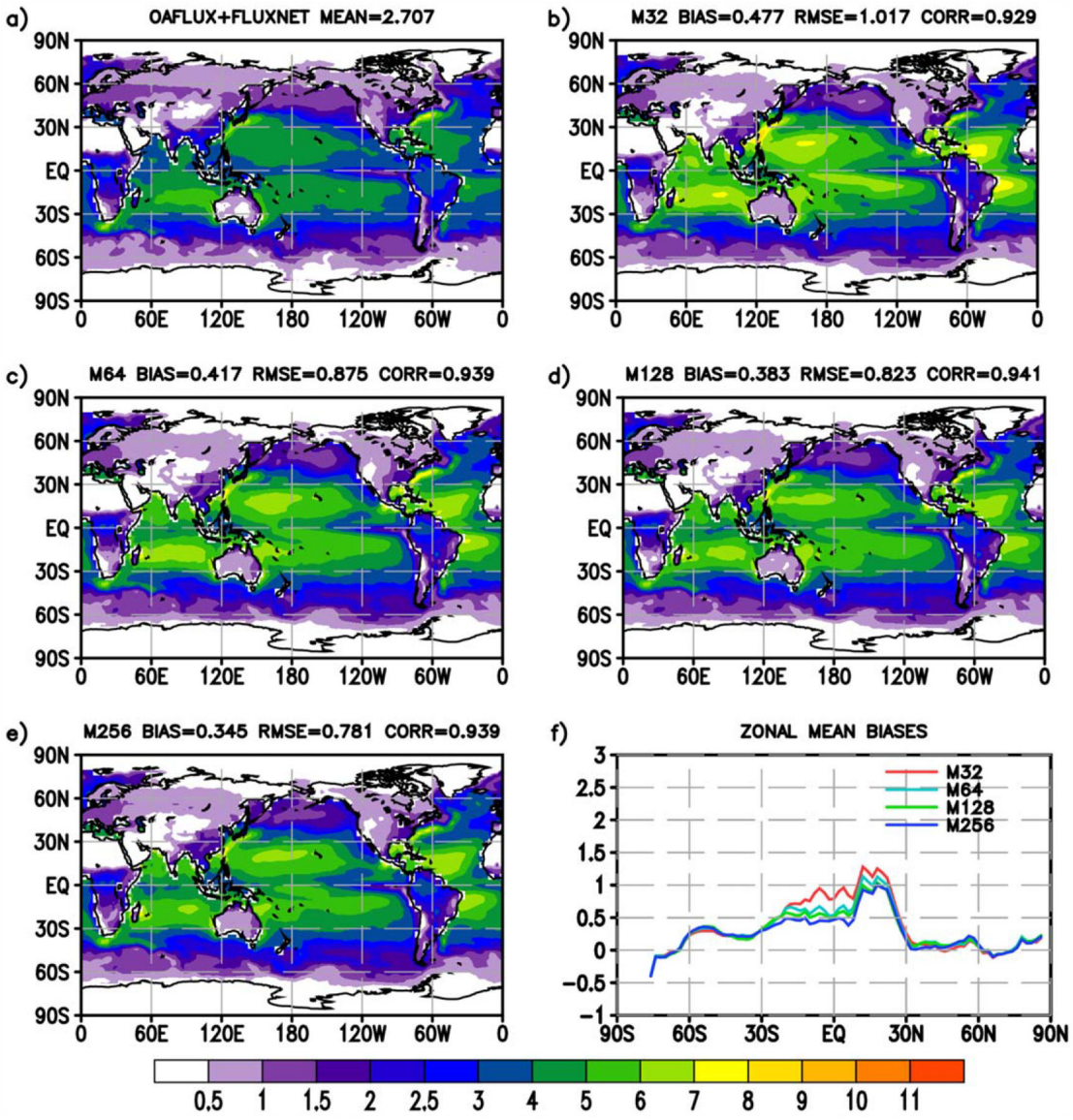

Figure 7.

Two-year (2007–2008) mean surface evaporation rate (mm d^{-1}) from (a) the combination of OAFlux (over ocean) and FLUXNET (over land) observations and the (b) M32, (c) M64, (d) M128, (e) M256 simulations. The GMMF zonal mean biases are given in Figure 7f with red, light-blue, green, and dark-blue lines for the M32, M64, M128, and M256 experiments, respectively.

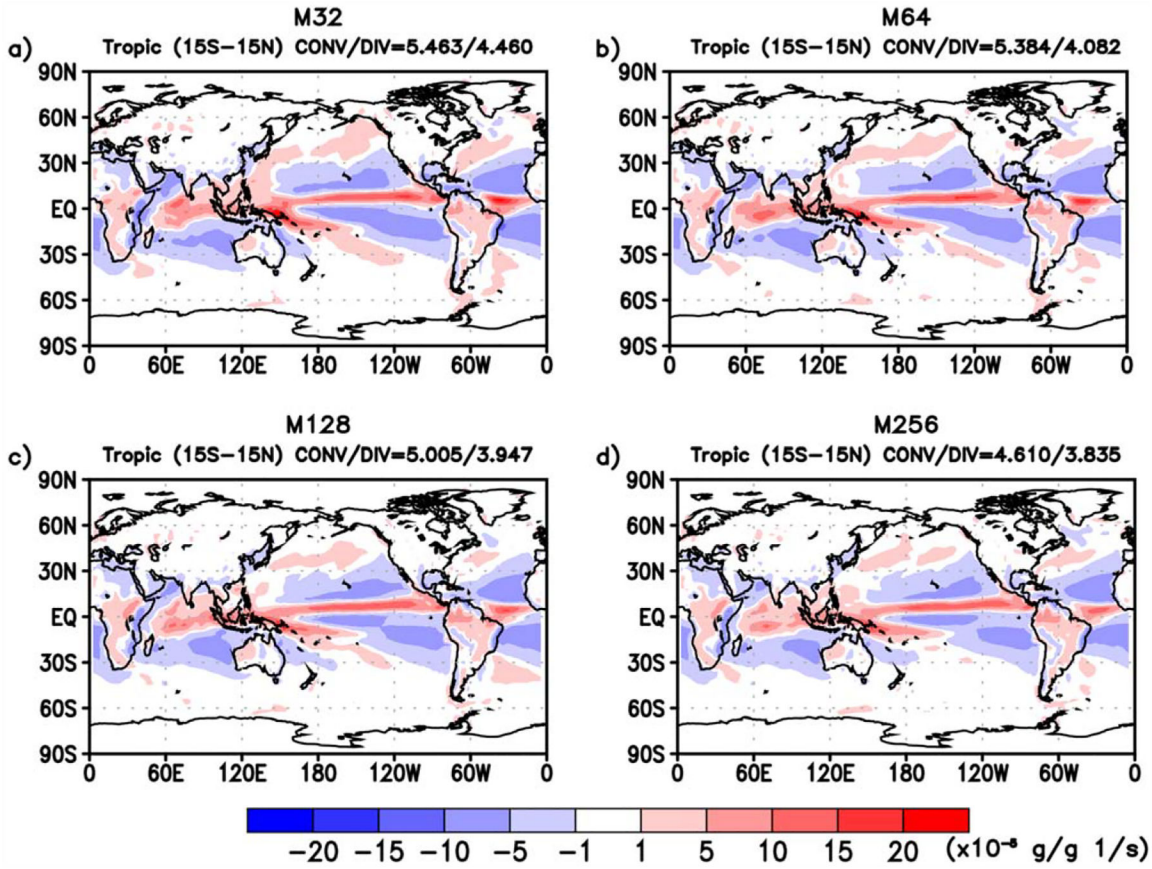

Figure 8.

Annual mean low-level (i.e., surface to 700 hPa) moisture flux convergence ($\times 10^{-5}$ g g^{-1} s^{-1}) from the (a) M32, (b) M64, (c) M128, and (d) M256 GMMF experiments. The mean moisture flux convergence/divergence amplitude over the Tropics (15°S–15°N) is also given at the top of each plot.

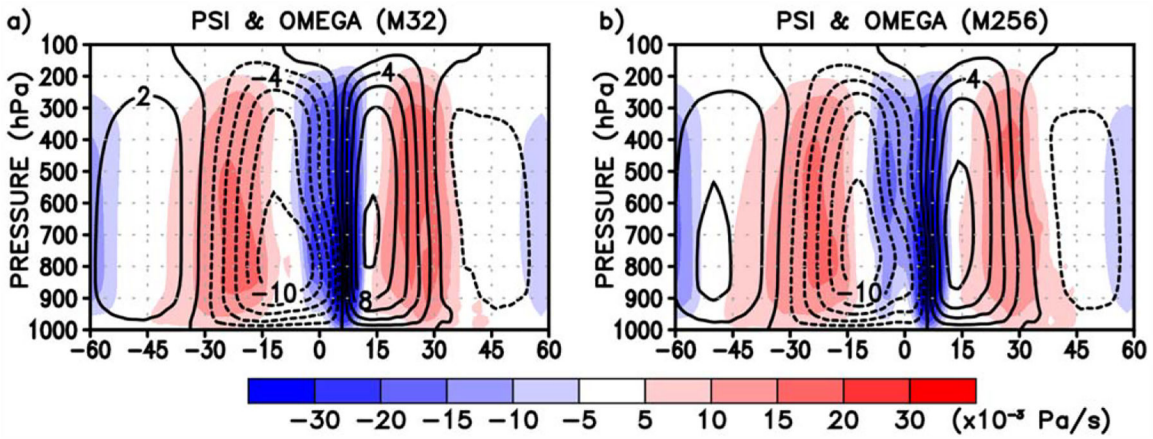

Figure 9.

Annual average zonal mean meridional mass stream function values (contours) overlapped with mean vertical pressure velocity (color shading) from the a) M32 and b) M256 GMMF simulations. Units for mass stream function and vertical pressure velocity are 10^{10} kg s^{-1} and 1.0^{-3} Pa s^{-1}, respectively. Positive (solid contours) and negative (dashed contours) stream function values represent counterclockwise and clockwise circulations, respectively.

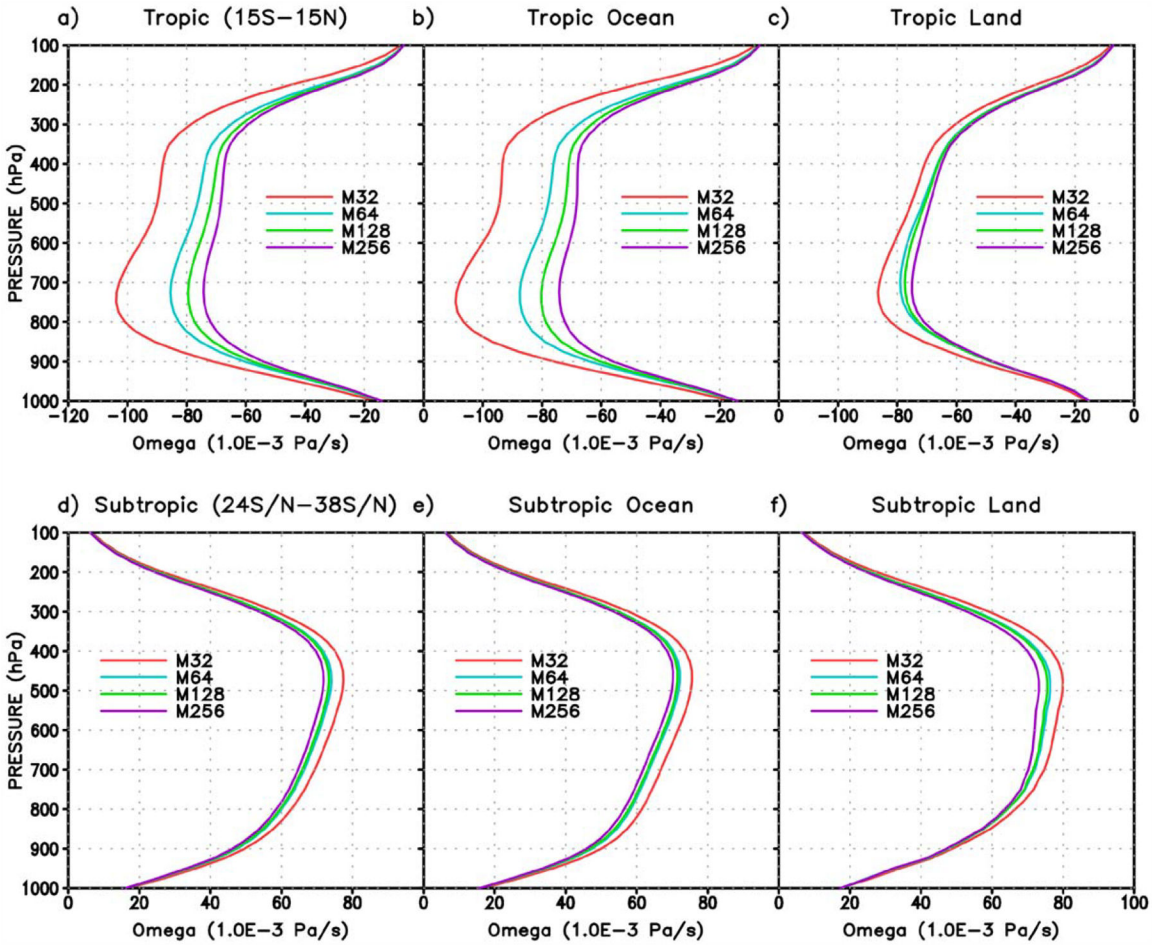

Figure 10.

Two-year (2007–2008) mean vertical pressure velocity (1.0^{-3} Pa s^{-1}) for GCM model cells with updrafts from the M32, M64, M128, and M256 GMMF simulations over (a) the Tropics (15°S–15°N), (b) tropical ocean, (c) tropical land and for GCM model cells with downdrafts over (d) the subtropics (24°S/N–38°S/N), (e) subtropical ocean, and (f) subtropical land.

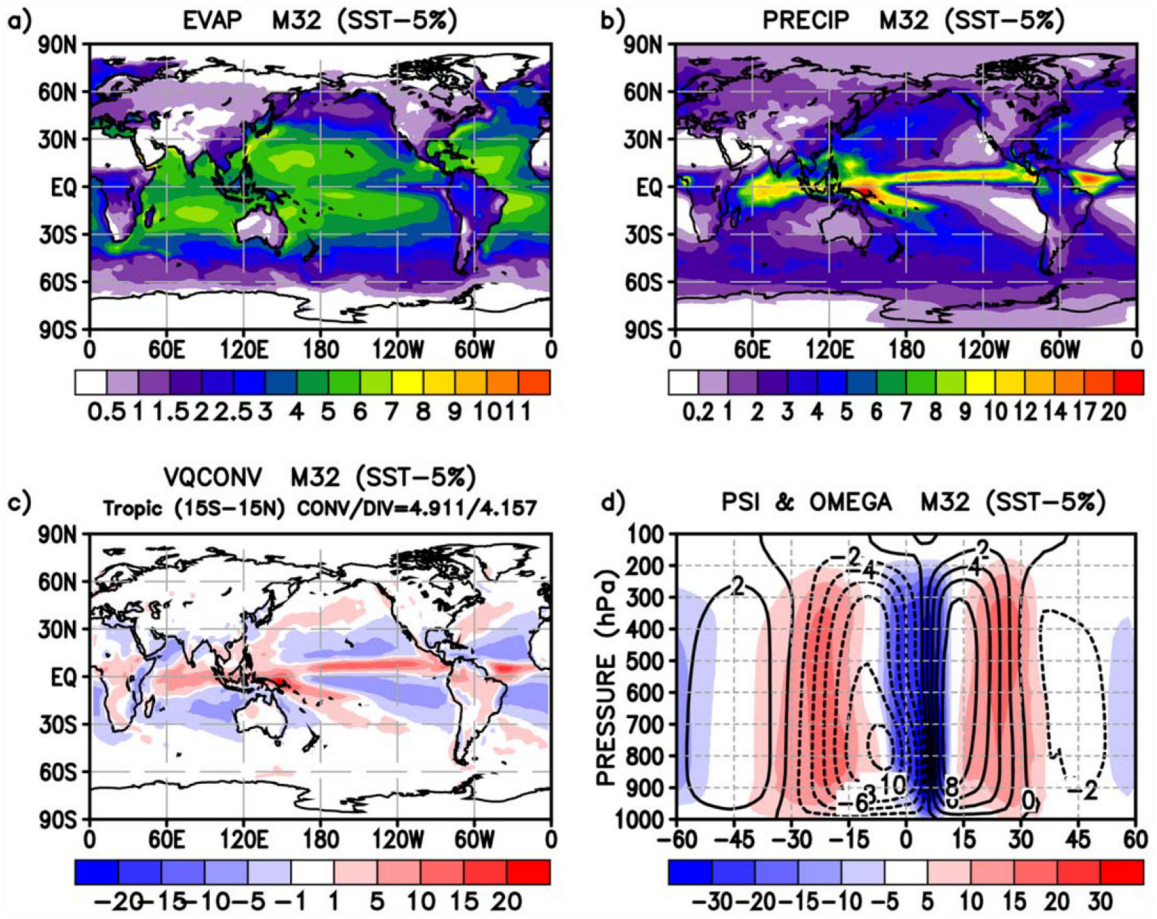

Figure 11.

Two-year (2007–2008) annual mean (a) evaporation rate (mm d^{-1}), (b) precipitation rate (mm d^{-1}), (c) low-level moisture flux convergence ($\times 10^{-5}$ g g^{-1} s^{-1}), and (d) zonal mean meridional mass stream function values (contours) overlapped with mean vertical pressure velocity (color shading) from the GMMF sensitivity experiment with SSTs (in °C) reduced by 5%. Units for mass stream function and vertical pressure velocity are 10^{10} kg s^{-1} and 1.0^{-3} Pa s^{-1}, respectively.

Table 1.

Key MMF Papers and Their Model Configuration in Terms of GCM Resolution and Number of Embedded CRM Grid Columns and Their Resolution[a]

Reference	GCM Resolution	CRM (# ofGrid/ Resolution)	Period of Model Integration	Total Rainfall (West Pacific and Tropics)
Khairoutdinov et al. [2005]	T42 (~300 km)	64/4 km	500 days	Overestimated for 2-D
		8 × 8/4 km		Better but underestimated for 3-D with momentum
Luo and Stephens [2006]	T42 (~300 km)	64/4 km	10 months	Overestimated
Ovtchinnikov et al. [2006]	T42 (~300 km)	64/4 km	1999 (SGP/TWP)	Overestimated and underestimated
Wyant et al. [2006, 2009]	2.8° × 2.8°	32/4 km	3.67, 5.25 year (+2K SST)	N.A.
DeMott et al. [2007, 2010]	T42 (~300 km)	64/4 km	500 days 1986–1999	Overestimated
Zhang et al. [2008]	2.0° × 2.5°	64/4 km	1998–2002	Overestimated
Khairoutdinov et al. [2008]	T42 (~300 km)	32/4 km	1985–2004	Overestimated
Kim et al. [2011]				
Benedict and Randall [2009]	2.5° × 2.5°	32/4 km	1985–2004	Overestimated
Thayer-Calder and Randall [2009]	2.0° × 2.5°	64/4 km	1998–2002	Overestimated
Marchand et al. [2009]	2.0° × 2.5°	64/4 km	1997–2002	Overestimated
Pritchard and Somerville [2009]	T42 (~300 km)	32/4 km	2000–2006	Overestimated
Zhu et al. [2009]	T42 (~300 km)	32/4 km	1998–2002	Overestimated
Marchand and Ackerman [2010]	2.0° × 2.5°	64/4 km and 64/1 km	1 year and 1 month	N.A.
Stan et al. [2010]	T42 (~300 km)	32/4km	22 years	Overestimated
Stan et al. [2010][b]	T42 (~300 km)	32/4 km	1979–2006	Overestimated
Dirmeyer et al. [2012]	(CCSM)		1998–2009	
Benedict and Randall [2011]	2.8° × 2.8°	32/4 km	1999–2004	Overestimated
	1-D Slab Ocean			
Cheng and Xu [2011]	T21 (~400 km)	32/4 km	1990–1992	Underestimated (Compared to *Legates and Willmott* [1990])
DeMott et al. [2011]	T42 (~300 km) (CCSM&CAM)	32/4 km	1986–2003	Overestimated (Summer) (Less in CCSM)
Pritchard et al. [2011]	1.9° × 2.5°	64/1 km	3 months	Overestimated (USA)
Wang et al. [2011, 2012, 2015]	1.9° × 2.5°	32/4 km	32, 52 months	Overestimated (no aerosol)
Goswami et al. [2011, 2013]	T42 (~300 km)	32/4 km	1997–2008	Overestimated
Rosa et al. [2012]	1.9° × 2.5°	64/2 km	1996–2006	Overestimated
Rosa and Collins [2013]	2.0° × 2.5°		1996–2001	
Li et al. [2012]	1.875° × 2.0°	64/2 km	1996–2001	Overestimated (USA)
Wyant et al. [2012]	2.8° × 2.8°	32/4 km N/S	Climate (4 × CO_2)	N.A.
Kooperman et al. [2012]	1.9° × 2.5° with nudging and aerosol	32/4 km	1 year	Overestimated
DeMott et al. [2013]	T42 (~300 km) (CCSM)	32/4 km	1998–2010	Overestimated

Reference	GCM Resolution	CRM (# ofGrid/ Resolution)	Period of Model Integration	Total Rainfall (West Pacific and Tropics)
Xu and Cheng [2013a,b]	1.9° × 2.5°	32/4 km	Last 9 year of 10year integration	Overestimated
Cheng and Xu [2014]	T21 (~400km)	32/4 km	1990–1992	See text
Pritchard and Bretherton [2014]	T42 (~300 km)	32/4 km	1980–1986	N.A.
Stan and Xu [2014]	1.9° × 2.5°	32/4 km	1979–2010	Overestimated
	0.9° × 1.25°	32/3 km		
Pritchard et al. [2014]	T42 (~300 km)	32/4 km	1980–1990	Overestimated
		16/4 km		
		8/4 km		
Tao et al. [2009]	2.5° × 2.0°	32/4 km	1998–1999	Overestimated
Tao et al. [2014]	2.5° × 2°	32/4 km	1998–2013	Overestimated
Mohr et al. [2013]	2.5° × 2°	32/4 km	2007–2008	Overestimated
Kidd et al. [2016]	2.5° × 2.0°	64/4 km	2007 (nudged to ERA-Interim)	Underestimated
Chern et al. [2016]	2.5° × 2.0°	32/4 km	2007–2008	Overestimated
Matsui et al. [2016]		64/4 km	June 2008	Overestimated
	2.5° × 2.0°	32/4 km	2007–2008	Overestimated
		64/4 km		
		128/2 km		
		256/1 km		

[a]The period of model integration and the precipitation bias are also shown.

[b]See *Dirmeyer et al.* [2012].

Table 2.

Experiment Name and Model Configuration for 4 GMMF (M32, M64, M128, and M256) and 4 GCE Simulations (C32, C64, C128, and C256). The GEOS Grid Spacing is 2.5° and 2.0° in Longitude and Latitude, Respectively

	CRM Grid Columns	CRM Grid Spacing	CRM Domain Size	GEOS Grid Spacing	Time Integration
M32	32	4 km	128 km	2.5° × 2°	2 years
M64	64	4 km	256 km	2.5° × 2°	2 years
M128	128	2 km	256 km	2.5° × 2°	2 years
M256	256	1 km	256 km	2.5° × 2°	2 years
C32	32	4 km	128 km	No	10 days
C64	64	4 km	256 km	No	10 days
C128	128	2 km	256 km	No	10 days
C256	256	1 km	256 km	No	10 days

Table 3.

Convective, Stratiform, and Total Rainfall (in mm d^{-1}), the Stratiform Fraction (%), Temporal Correlation, and Domain-Mean Rainfall Bias for the C32, C64, C128, and C256 Experiments

	C32	C64	C128	C256
Convective (mm d^{-1})	5.52	5.63	6.35	6.25
Stratiform (mm d^{-1})	7.34	7.67	7.04	7.01
Stratiform (%)	57	57	53	53
Total Rainfall (mm d^{-1})	12.86	13.37	13.39	13.26
Correlation	0.73	0.79	0.84	0.90
Bias (mm d^{-1})	−0.17	0.33	0.36	0.23

Table 4.

Total Global Precipitation, Tropical Rainfall and Its Convective and Stratiform Components (in mm d^{-1}), and Stratiform Percentage From the M32, M64, M128, and M256 Experiments[a]

	M32	M64	M128	M256
Global total Precipitation (mm d^{-1}) (90°S-90°N)	2.93	2.89	2.86	2.83
Tropical rainfall (mm d^{-1}) (38°S-38°N)	3.27	3.20	3.17	3.12
Tropical convective rainfall (mm d^{-1}) (38°S-38°N)	1.466	1.568	1.324	1.169
Tropical stratiform rainfall (mm d^{-1}) (38°S-38°N)	1.804	1.637	1.849	1.956
Tropical stratiform percentage (%) (38°S-38°N)	55	51	58	63
Correlation (GMMF and GPCP)	0.817	0.814	0.839	0.842
Correlation (GMMF and TRMM 3A25)	0.825	0.825	0.851	0.857
Bias (versus GPCP)	0.27	0.23	0.20	0.17
Bias (versus TRMM 3A25)	0.36	0.30	0.26	0.22
RMSE (versus GPCP)	1.74	1.66	1.47	1.37
RMSE (versus TRMM 3A25)	1.85	1.75	1.54	1.42

[a]Two sets of spatial correlation, bias, and root-mean-square error (RMSE) are computed between the GMMF simulations and TRMM 3A25 (38°S–38°N) and GMMF simulations and GPCP (90°S–90°N) products, respectively.

Table 5.

GMMF-Simulated Global and Regional Mean Surface Precipitation and Evaporation Rates (mm d^{-1})[a]

	Observations	M32	M64	M128	M256
Global total precipitation rate (mm d^{-1})	2.659	2.931	2.885	2.860	2.830
Global total precipitation rate (mm d^{-1}) from ocean	2.001	2.424	2.359	2.326	2.293
Global total precipitation rate (mm d^{-1}) from land	0.662	0.507	0.526	0.534	0.537
Precipitation rate (mm d^{-1}) over tropical ocean (15°S-15°N)	3.769	5.782	5.611	5.380	5.248
Global total sfc evaporation rate (mm d^{-1})	2.708	2.979	2.923	2.892	2.858
Global total sfc evaporation rate (mm d^{-1}) from ocean	2.350	2.702	2.633	2.598	2.556
Global total sfc evaporation rate (mm d^{-1}) from land	0.382	0.277	0.290	0.294	0.302
Sfc evaporation rate (mm d^{-1}) over tropical ocean (15°S-15°N)	3.592	5.255	4.931	4.815	4.686

[a]Observed precipitation and evaporation rates over ocean and the evaporation rate over land come from GPCP, OAFlux, and FLUXNET, respectively. For surface evaporation, the same OAFlux observation points over ocean and FLUXNET points over land are used in the GMMF calculations (i.e., observed missing points are omitted in the GMMF).